The accumulation of molten volcanic ash in jet engines; simulating the role of magma composition, ash particle size and thermal barrier coatings.

David Pearson and Richard Brooker*

School of Earth Sciences, University of Bristol, Wills Memorial Building, Queens Road, Bristol, BS8 1RJ, UK. (* corresponding author, e-mail Richard.brooker@bristol.ac.uk)

ABSTRACT

As the eruption of Icelandic volcano Eyjafjallojökull demonstrated in 2010, volcanic ash can cause major disruption to commercial aviation. The primary concern is related to the build-up of ash deposits in aircraft gas turbine engines which can critically interfere with the carefully balanced internal flow regime, leading to loss of engine thrust with potentially dire consequences. As a result, limits are placed on the acceptable ash exposure (dose) for commercial aircraft flying in and around eruptive events. The role of ash composition is known to be an important variable but the rate of deposit build-up, the nature of the deposits and how this is affected by interaction with ceramic thermal barrier coatings is not well understood.

In this study, volcanic ash samples from seven compositionally diverse volcanoes were heated and deposited onto coated and uncoated Nimonic alloy targets at temperatures matching those of modern engines currently in service. Measurements of the mass and volume of the ash deposits are used to calculate the key parameters that would create a reduction in the flow passage area at the High Pressure Nozzle Guide Vanes (HPNGV). For the realistic range of fine ash sizes tested (median diameter 4 to 40 μm, up to a maximum at 125 μm), there is a clear trend of increasing deposition rate with increasing particle diameter. After correcting for particle size, there is no clear influence of ash composition on the rate of build-up of deposit in terms of mass. However, an important finding from our study is that ash from more silicic volcanoes forms a relatively low density deposit, with significant vesicularity, implying an increased level of reduction of flow area for a given mass of ash deposit on the HPNGVs. It is also clear that ash remains adhered to ceramic coatings more efficiently than bare metal and we find that low silica ash is the most likely to penetrate in to the thermal barrier coating and the least likely to be dislodged by temperature reduction.

Highlights

- Ash particle size has a very significant influence on mass deposition rate
- Deposits on ceramic Thermal Barrier Coatings do not detach so easily on cooling
- High-silica deposits cause more blockage at a given mass dose, due to higher porosity
- Low-silica deposits are most likely to remain attached on cooling
- We present a method for predicting deposit thickness for given ash exposure scenarios

Keywords

Volcanic ash, Jet engines, Aviation hazard, Thermal Barrier Coating.

1. Introduction

As gas turbine powered aircraft encounter ash from volcanic eruptions, the primary safety concern is the potential risk of multi-engine surge rendering some or all of the engines simultaneously inoperative. Two of the more publicly documented incidents involved Boeing 747 aircraft losing thrust from all four engines after flying through ash clouds generated by Mt Galunggung, Indonesia in 1982 and Mt Redoubt, USA, 1989 (Casadevall, 1994, Dunn 2012). Luckily, in each of these events the aircraft was able to regain sufficient thrust to land safely. Events such as these led to new advisory regulations that in April 2010 resulted in the cancellation of over 10,000 flights due to the ash cloud created by the eruption of the Icelandic volcano Eyjafjallojökull (Brooker 2010, Langmann et. al., 2012). This event placed some operators within hours of bankruptcy and total losses are estimated at around $1.8 billion for airline and related businesses (IATA, 2010), prompting a close look at the exact levels of ash a jet engine might tolerate.

When an aircraft flies through an ash cloud, the ash/air mixture is drawn through the engine fan and compressors and then into the combustor (Figure 1.a). The ash will encounter very high temperatures created by the burning air/fuel mixture. Heat is transferred to the ash which becomes partially or totally molten, as it is carried by the gas flow in to the turbine section of the engine (Przedpelski & Casadevall, 1991, Giehl et. al., 2017). At the exit of the combustion chamber the hot gas/ash mixture must pass through the High Pressure Nozzle Guide Vanes (HPNGVs) (see Figure 1.b&c). The shape of the channels formed between adjacent HPNGVs are critical to the efficient and stable operation of the engine. In particular, if this area becomes restricted and flow is reduced, the engine has an increased likelihood of surge (the sudden reversal of flow within the engine resulting in a major or total loss of thrust).

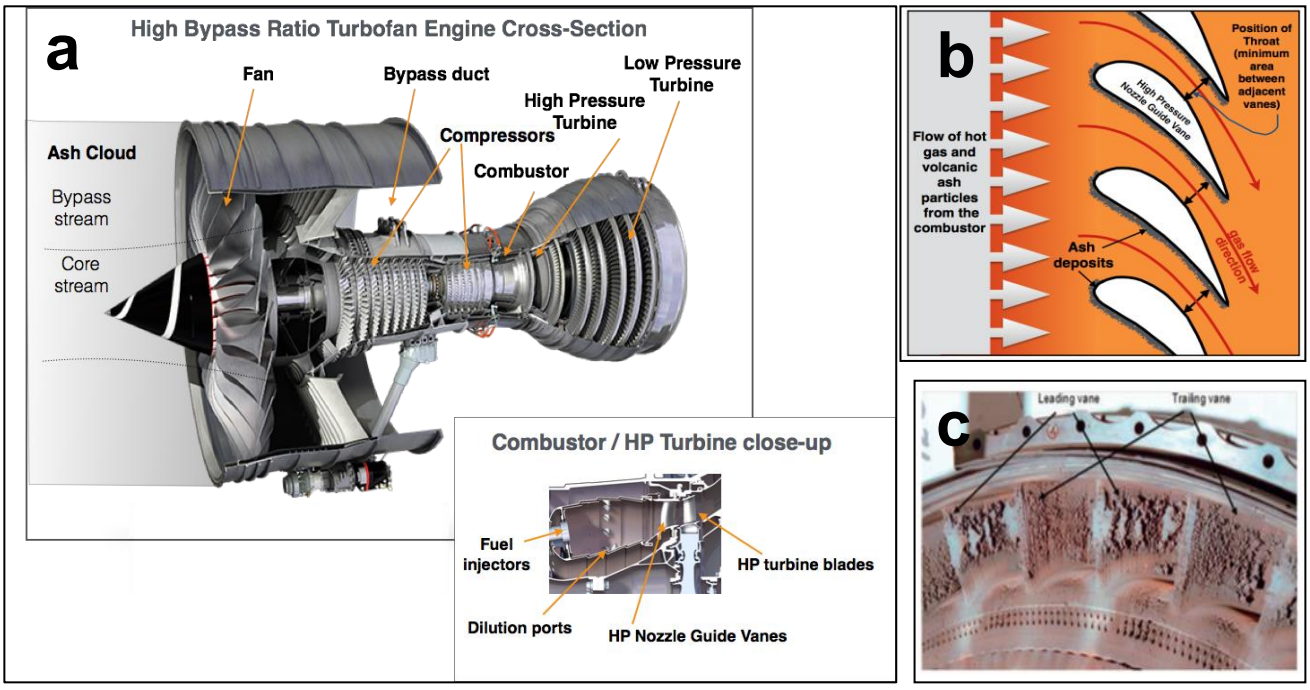

Figure 1. a; *Cross section of a modern aircraft jet engine (RR Trent). Image copyright Rolls-Royce plc.* ***b;*** *Schematic view of High Pressure Nozzle Guide Vanes (HPNGVs).* ***c;*** *Volcanic ash build-up on the HPNGVs of an engine which encountered ash from Mt. Gulanggung, Indonesia,1982 (Clarkson et.al.,2016)*

The build-up of volcanic ash deposit is dependent upon a number of variables. Some of these factors relate to the physical conditions within the engine (e.g. temperature and velocity) while others

pertain to the composition and make-up of the ash (e.g. silica content, crystal vs glass content, particle size) (Giehl et. al., 2017, Song et. al., 2016; Wiley et al., 2016).

Historic incidents where engine surge has been reported are shown on a total alkali vs silica (TAS) diagram in Figure 2.a. This limited sample size of engine events suggests that severe HP NGV blockage that could lead to surge, has occurred over the range of 50% to 60% silica. This finding is not unexpected as the majority of volcanic eruptions that inject a large quantity of fine ash in to the atmosphere occur with this type of magma chemistry.

However, it is possible for lower silica content basaltic magmas to create large quantities of fine ash, particularly due to magma-water interaction during the eruption (Gonnerman, 2015). Equally, higher silica content magmas such as Dacite and Rhyolite could create large volumes of fine ash, albeit generally associated with large eruptions which occur relatively infrequently.

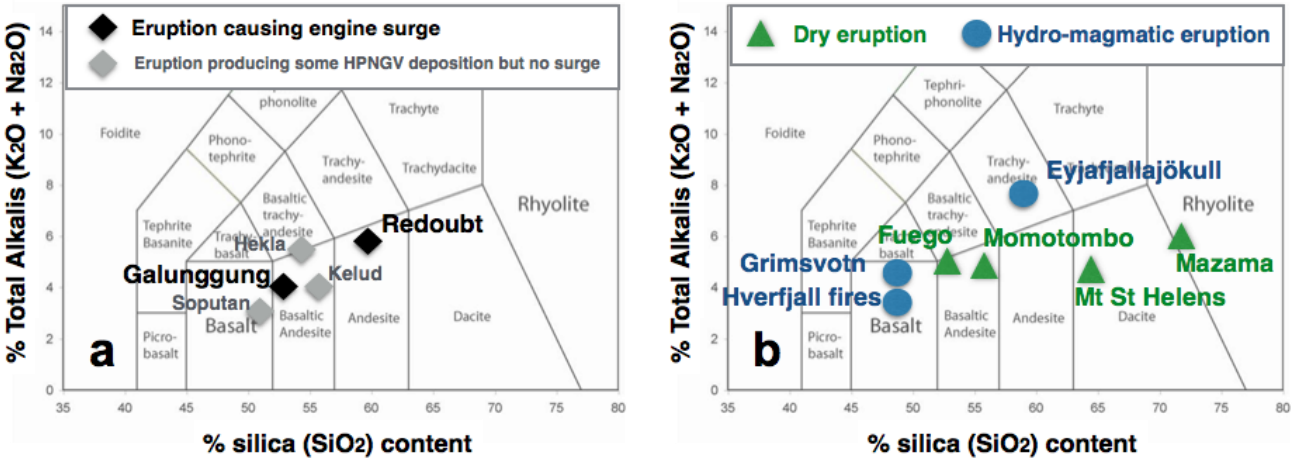

Figure 2. a; *Eruptions that have caused engine surge and/or damage positioned on a total alkali vs silica content (TAS) plot. The magma type classification is shown (Le Bas et al., 1986).* ***b;*** *The seven volcanoes used in this study positioned on a total alkali vs silica content (TAS) plot.*

Flight safety rules have largely been built on experience from historic events, particularly the Redoubt and Galunggung encounters. In order to provide data to help refine this approach and to determine whether such rules should be modified to account for other magma types, we have undertaken a series of laboratory experiments using ash from a wide range of volcanic eruptions (Figure 2.b). These tests focus on the melting and deposition behaviour of the ashes at temperatures similar to those encountered within aircraft gas turbine engines.

In this study we build on the experimental method of Giehl et al. (2017) to investigate which variables might be important in controlling the rate of build-up of molten ash deposits. Although it is impossible to fully replicate the conditions inside a gas turbine engine in the laboratory, these experiments have been carried out with representative ash samples, deposition surface materials and coatings. Realistic heat transfer times and deposition surface temperatures are achieved in the experiments and other scaling factors are critically evaluated.

2. Previous Work

Important parameters to consider in this study include the mass and rate of ash entering the system, the physical and chemical characteristics which determine how easily it becomes molten and the way

it builds up on the HPNGVs. In response to the 2010 crisis, the aviation community agreed to allow flights in 'low dose' volcanic ash clouds (of generic composition) as long as the concentration remained below 2 mg/m^3 (Clarkson et. al., 2016). More recently, pressure has grown on aircraft gas turbine engine manufacturers to better understand and define the risks created by the full range of volcanic ash scenarios. Models for determining the effect of ingested volcanic ash on compressor surge have been created in order to better quantify these effects (Clarkson and Simpson, 2017). Understanding the processes acting upon the volcanic ash as it passes through the engine is key to improving the fidelity of these models.

The melting characteristics of a range of ash samples have been evaluated and found to show significant variation (Swanson and Beget, 1991; Giordano et.al., 2005; Song et.al., 2016, Giehl et al., 2017)). These studies show that melting of volcanic ash occurs over a wide temperature range due in part to the fact that ash clouds contain a number of different particles including crystals, glass and lithics of different shapes and dimensions (Cashman and Rust, 2017). Several studies indicate that the mass of ash deposited on a hot surface is dependent upon the magma composition from which the ash was formed with low silica lavas (basalts and basaltic andesites) having the highest propensity for adhesion (Giehl et. al., 2017, Dean et.al. 2016, Song et.al., 2016). As the volume occupied by the deposit defines the blockage in the HPNGV passages, the density of the deposit is as critical as the mass deposition rate in assessing the effects of the ash on the engine. This aspect has been less well studied. Actual observations of the density of ash deposits in jet engines are scarce and limited to the examination of engines after volcanic ash encounters (Dunn, 2012, Clarkson et. al, 2016).

Various studies have also examined how the size of ash particles influences likelihood of deposition (Giel et. al.,2016, Taltavull et.al., 2016, Bonilla et.al., 2012, Wylie et. al., 2016). These studies suggest that very fine particles (solid or molten) may not impact the engine parts as they follow the gas flow around objects, while very large particles can bounce off without adhering as they are more difficult to melt in a given combustor exposure time. These observations are confirmed by computational fluid dynamics (Jiang et. al., 2017). The most likely particle size distributions of ash entering the engine compressors is well understood and corroborated by physical measurements and predictive models. Ash clouds with median particle sizes of 20 to 50 μm are typical of those likely to be encountered by aircraft (Prata, 2009, Bonadonna et. al., 2011). It is also recognised that the particle size distribution is modified as ash passes through the engine due to multiple high-energy impacts, particularly with the rotating aerofoils in the compressor section of the engine. This effect has been quantified by comparing the particle size distributions observed in engines after exposure to volcanic ash (Dunn, 2012, Lekki & Woike, 2017) and indicates a size reduction by a factor of 5 could be involved.

The hot turbine components in most modern gas turbine engines are complex metal alloys which are often ceramic coated in order to increase resistance to thermally induced stresses, creep and corrosion (Clarke et. al., 2012). A number of studies have shown that the presence of even minor volcanic ash deposits can degrade the long-term effectiveness of these coatings due to interference with the microstructure of the coating (Lee et. al., 2014, Mechnich et. al., 2011, Patnaik, et. al., 2017, Naraparaju, et al., 2018). These coatings may also influence the deposition behaviour of volcanic ash as they modify the surface properties on to which the ash is deposited (Song et. al.,2019).

3. Methods and materials

3.1 Ash deposition apparatus

The experimental apparatus is similar to that used by Giehl et al., (2017) as illustrated in Figure 3.a. An oxy-acetylene welding torch is mounted within a metal safety enclosure. The flame from the torch is directed on to a target held by a clamp. The angle of the target can be varied. However, for these

experiments a constant incidence angle of 45° was used throughout. The targets are made from Nimonic 75 material, a nickel-based metal alloy used for the manufacture of high temperature turbine components. The dimensions of the targets are 60mm x 15mm x 1.6mm (length x width x thickness). Two types of target are used, **Uncoated:** Bare metal Nimonic 75, and **Coated:** Nimonic 75 with a thermal barrier coating comprised of a 0.1 to 0.15 mm thick layer of yttria stabilised (7%) zirconia deposited by plasma vapour on an aluminium base coat (Figure 7.a shows a section through the target highlighting the structure and surface texture of the coating before exposure to ash).

The ash is introduced through a primary funnel on to a distributor plate. Vibration is applied by an electric motor with an eccentric mass. The speed of the motor is controlled to aid an even particle separation and flow. The ash is passed in to a small glass funnel which is aligned directly over the flame 7 mm from the torch outlet. At the start of each test the welding torch is adjusted to obtain the required gas temperature at the surface of the target measured with an S-type thermocouple. The thermocouple is then removed. Ash is introduced to the funnel at a target rate of 0.02 g per minute. Ash that falls through or around the flame is collected on a tray. The mass of this 'fall-through' ash and any remaining on the funnel is weighed to calculate the mass of ash input to the flame. After the introduction of the ash, the target is usually maintained at temperature for two minutes before the torch is extinguished. However, in a few experiments the torch was left heating the deposit for a further 60 minutes without more ash being added and in some cases the target was slowly moved away from the flame to give post-deposition cooling at a pre-calibrated rate.

During cooling, a large metal tray is placed below the target to ensure that any deposit that detaches during the cool-down period is collected. The detached deposit is weighed and retained for analysis. The target is weighed before and after the test. The total mass of deposit is calculated by adding the increase in mass of the target and the mass of detached deposit. For all tests the distance from the torch outlet to the target surface, measured along the horizontal centreline of the torch flame, is set at 67 mm (± 1 mm). A temperature of 1250 °C (±5 °C) at the target surface is used unless otherwise stated.

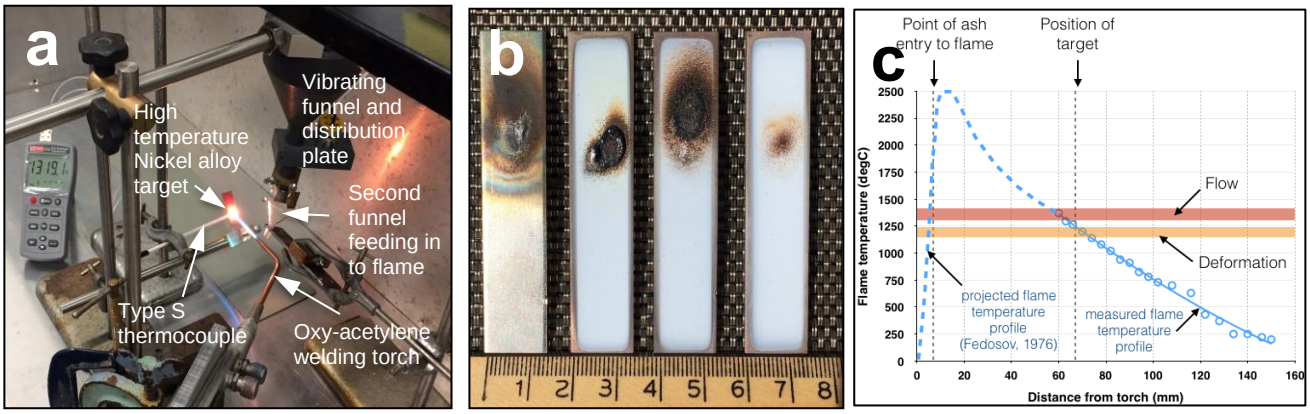

Figure 3. a; *The experimental set-up.* ***b;*** *Targets after cool-down (left to right: uncoated target with Fuego ash, coated target with Grímsvötn ash, coated target with Eyjafjallajökull ash, coated target with Mazama ash (scale in cm).* ***c;*** *Results of the flame temperature calibration. 'Flow' and 'Deformation' are the ash melting temperatures of Song et al., 2016 which probably represent sub- and super-liquidus conditions above the glass transition (Tg).*

3.2 Temperature & velocity

The temperatures in the flame are plotted as a function of distance from the torch outlet in Figure 3.c. The blue circles and solid blue line on this plot represent the measured data while the dotted line is the acetylene flame data of Fedosov (1976). Also shown are the positions of ash entry to the flame and the target. The plot indicates the range of temperatures at which 'deformation' and 'flow' of a range of volcanic ash types was measured by Song et. al., 2016 (see supplementary material A). The target surface temperature of 1250 °C used in these experiments lies between these two temperatures. High speed video is used to determine particle velocity. A Phantom HSV camera was mounted above the target, viewing vertically downwards. High speed video (2900 fps) allows velocity to be determined by counting the number of frames taken for a particle to travel from the torch entry point to the target, typically giving 12 to 15 ms^{-1} regardless of the particle size or composition.

3.3 Ash characterisation

Ash samples from seven different volcanoes cover the range of silica and crystal content listed in Table 1 and plotted in Figure 2.b. The samples were collected from deposits in the field and most have been analysed by other researchers to determine their crystal content and morphology (see Table 1). Ash samples containing large particles are sieved to below 125 μm in order to be more representative of the size likely to be encountered in distal ash clouds. Ash from both 'dry' and hydro-magmatic eruptions are included to represent the types of eruption that cause high levels of fragmentation and large volumes of fine ash particles (Gonnerman, 2015, Kaminski and Jaupart, 1998, Wohlentz et. al., 2013). To simulate the effect of size reduction within the engine, a number of the ash samples were reduced in size using a ball mill. The particle size distributions of all ash samples were measured using a Malvern Mastersizer (type R). The size distributions are summarised in Table 1 and shown in supplementary material B. More details for individual ash samples are given in the results section.

Table 1. Summary of the properties of the ash samples tested.

Ash sample	Volcano	Magma type	% SiO_2 bulk magma	% crystals	Hydro-magmatic	Sieved to <125 μm	D_{10} (μm)	D_{50} (μm)	D_{90} (μm)	Milled ash	D_{10} (μm)	D_{50} (μm)	D_{90} (μm)
Hve	Hverfjall fires	Basalt	50%	5%	yes	yes	8	47	105	**x**	<1	5	19
Gri	Grímsvötn	Basalt	50%	5-10%	yes	no	16	43	73	**x**	<1	5	15
Fue	Fuego	Basaltic andesite	54%	40%	no	yes	9	43	85	**x**	<1	3	27
Mom 5am	Momotombo	Basaltic andesite	55%	25%	no	yes	4	13	80				
Mom 6am	Momotombo	Basaltic andesite	55%	40%	no	yes	5	21	85				
Eyj	Eyjafjallojökull	Trachy andesite	58%	5%	yes	no	5	25	110				
Msh	Mt St Helens	dacite	60-70%	30%	no	yes	5	22	85	**x**	<1	4	18
Maz	Mazama	Dacite/ Rhyolite	70-75%	5%	no	no	5	23	72				

D_{10}, D_{50} and D_{90} represent the particle diameters at which 10%, 50% and 90% of the ash is smaller than this value (see Supplementary Material B). Ash sample references Hve = Liu et.al., 2017; Gri = Liu et.al., 2015; Fue = Buckland et.al., 2018; Mom5am and Mom6am = Withoos, 2017; Eyj = Gislason et.al., 2011; Msh = Eychenne et.al., 2015; Maz = Bacon et.al., 2006. The %SiO_2 composition is 'nominal' as bulk data is not provided for all the ash samples.

3.4 Deposit Characterisation

Digital photographs were used to record the overall shape of the ash deposits formed in the tests. These are taken from normal to the target surface (plan view) and in side view. Images taken at the

end of the ash deposition but prior to shut-down (before any detachment) are used to estimate the volume of the hot deposits. The exact method for this calculation is described in supplementary material C.

Cross-sections were cut through a number of the deposits either those that became detached or in a number of cases through the metal targets to include portions of the deposits that remain attached after cooling. These deposits were mounted in epoxy resin, then ground down and polished to a 1 μm finish. The mounts were carbon coated for analysis in a back-scatter mode using a scanning electron microscope (Hitachi S-3500N). High resolution digital images and X-ray micro-analysis (EDX) were obtained to determine the general composition of the deposits and record any features of particular interest such as crystal and bubble distributions.

4. Results

4.1 Deposition and Adhesion

4.1.1 Overall results and nomenclature

In this study, the term 'deposition' refers to the total maximum mass of hot ash accumulated on the target with the flame on, simulating a running engine in an ash cloud. The term 'adhesion' refers to the mass of ash remaining on the target after it has cooled to room temperature. The deposition volume is the key factor in triggering an engine surge while the adhesion data may be more representative of the deposit remaining after a surge has taken place and the engine has cooled or the aircraft has completed its flight.

In practical terms the 'total mass of ash deposit' is determined by measuring the sample still attached to the cooled target plus any which became detached **after** cooling. The 'mass of ash input' refers to the amount dropped into the flame minus any excess ash that fell straight through. It should be remembered that it is possible that some part of the 'mass of ash input' may not impact the target if it remains within the gas flow deflected around the target.

The deposition and adhesion rate for all experiments are summarized in Figure 4 which serves as an overall introduction. The results are subsequently presented in more detail for each ash type (Fig 5).

In Figure 4.a, the total mass of deposit is plotted against the mass of ash input. For reference, lines are plotted which represent a deposition rate of 100% and 20%. The data show that there is a significant variation in the deposition rate parameter with values ranging from 20 - 82%. Also shown is a 'limit dose' reference level of ash in the flame which is calculated to represent the mass of ash equivalent to an exposure of 2 hours in an ash cloud concentration of 2 mg/m^3, scaled to conditions of these experiments. The derivation of our 'limit dose' is described in the supplementary material D and represents the boundary of the Duration of Exposure vs Ash Concentration (DevAC) chart described by Clarkson et. al., 2016.

In Figure 4.b, the mass of deposit adhering to the target after cooling is plotted against the mass of ash input. The ratio of these two parameters is termed the adhesion rate. Again, reference lines are added to the plot. There is a significant variation in this parameter, generally ranging from 0 to 20% with one significant outlier at around 50%.

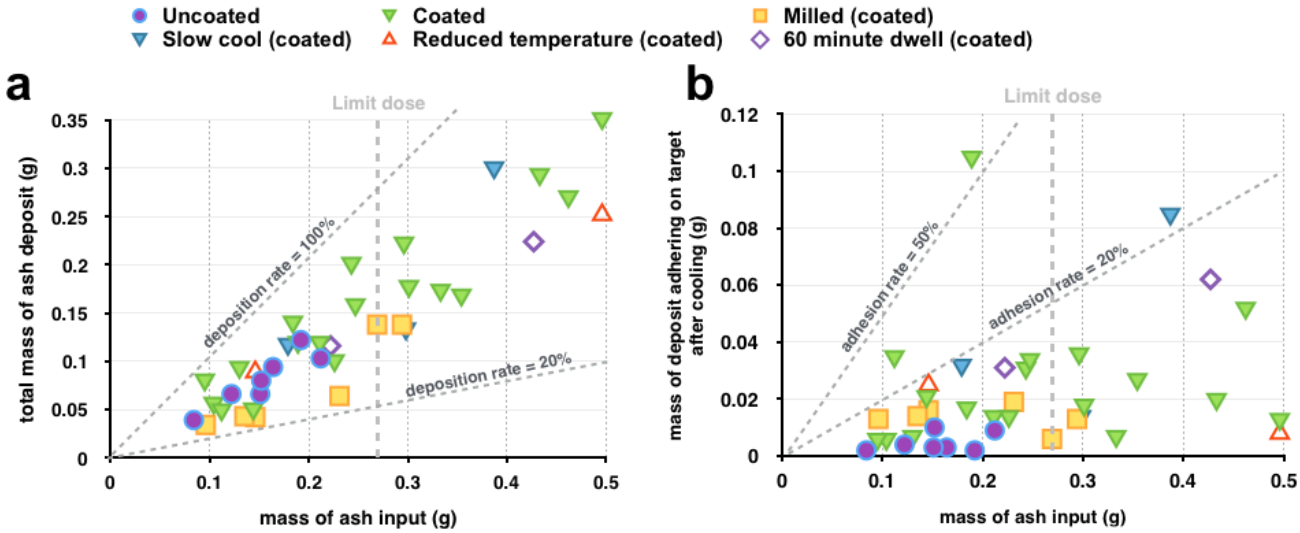

Figure 4. Summary deposition and adhesion data, a; *Total mass of the ash deposit vs the mass of ash input, reference deposition rates of 100% and 20% are shown.* ***b;*** *Mass of deposit adhering on the target after cooling vs the mass of ash input, reference adhesion rates of 50% and 20% are shown.*

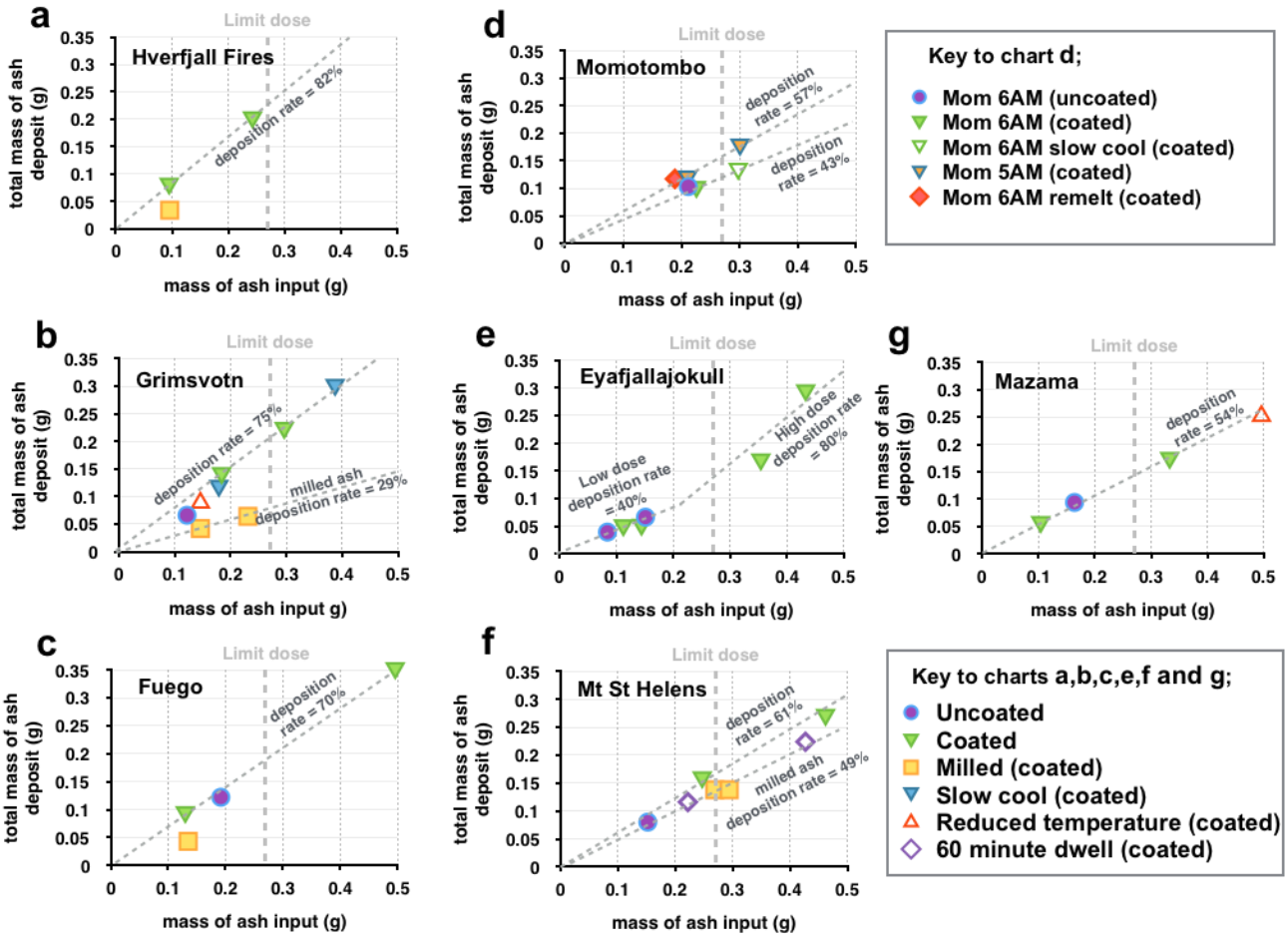

Figure 5. Deposition data for each ash type. *Total mass of the ash deposit vs the mass of ash input, the mean deposition rate for each ash type is shown.* ***a; Hverfjall Fires ash. b; Grímsvötn ash. c; Fuego ash. d; Momotombo ash. e; Eyjafjallojökull ash. f; Mt St Helens ash. g; Mazama ash.***

4.1.2 Hverfjall Fires ash (50% SiO_2)

Figure 5.a shows the deposition results for the Hverfjall Fires basaltic ash which is mostly glass with only a 5% crystal content. This sample from northern Iceland represents the opening tephra fall which created the Myvatn phreatomagmatic tuff cone 2500 years ago (Liu et. al., 2017). The ash has been sieved to remove particles greater than 125 μm. Some of the ash was milled for 5 minutes in a ball mill at 500 rpm. It should be noted that the age of this ash means it may have become hydrated which could influence its melt viscosity and sticking characteristics.

For the unmilled ash, there is extremely good agreement in the measured deposition rate of 82% in the two experiments with different total ash inputs. This glassy basalt has the highest deposition rate measured in all experiments, consistent with the results of Giehl et al., (2017). However, one test carried out with milled ash gave a much lower deposition rate of 37%. The adhesion rate after cooling for both unmilled and milled ash lies in the range 5 to 14%.

4.1.3 Grímsvötn ash (50% SiO_2)

Figure 5.b shows the deposition results for the Grímsvötn basaltic ash with 5-10% crystals. This sample from Southern Iceland is obtained from tephra fall from the phreatomagmatic eruption of 2011 (Liu et. al., 2017). The sample was collected 50 km from the vent and has not been sieved. Some of the ash was milled for 5 minutes in a ball mill at 500 rpm.

There is very good agreement in the relatively high deposition rate of 75% for the two experiments with the unmilled ash on coated targets. Two tests where the target was slowly moved away from the flame to give post-deposition cooling at a rate of around 100 °C per minute gave a similar mean deposition rate of 71%. However, one test carried out on an uncoated target gave a lower deposition rate of 54%. A single test with a lower target surface temperature of 1050 ^{o}C throughout deposition showed a deposit rate of 61%. The two milled ash experiments on coated targets are in good agreement with a measured deposition rate of 29%, again significantly lower than the unmilled sample.

The mean adhesion rate for unmilled ash on coated targets is 10%. This increases to 20% with a post-deposition cool down rate of 100 °C per minute. The adhesion rate with a reduced target surface temperature of 1050 $^{\circ}$C is also 20%. The experiment with unmilled ash on an uncoated target gave a very low adhesion rate of 3%. The mean adhesion rate for milled ash on coated targets was also 10%.

4.1.4 Fuego ash (54% SiO_2)

Figure 5.c shows the deposition results for the Fuego basaltic andesite ash which has 40% crystals. This sample from Guatemala was obtained from the upper section of a pyroclastic flow deposit which occurred during the paroxysmal dry eruption of September 2012 (Buckland et. al., 2018). The sample was collected 6 km from the vent and has been sieved to remove particles greater than 125 μm. The milled ash sample was created by milling a larger particle size fraction (0.125 to 0.25 μm) for 10 minutes in a ball mill at 500 rpm.

There is extremely good agreement in the measured deposition rate of 70% in the two experiments with the unmilled ash on coated targets. The test with an uncoated target gave a lower deposition rate of 64%. One test carried out with the milled ash (on a coated target) again gave a much lower deposition rate of 32%. The adhesion rate for unmilled ash on a coated target is very low, in the range 3 to 5%. However, this increases to 10% for the single test with milled ash, even though the deposition rate is lower.

4.1.5 Momotombo ash (55% SiO_2)

Figure 5.d shows the deposition results for the Momotombo basaltic andesite ash. The samples from this volcano in Nicaragua were obtained from tephra falling during a series of eruptions on 2nd December 2015. Two samples were collected at 5am and 6am. Both samples have been sieved to remove particles greater than 125 μm. The crystal contents of the 5am and 6am samples at this particle size fraction are 25% and 40% respectively (Withoos, 2017). A portion of the 6am ash sample was melted at 1400 °C in a platinum crucible then rapidly quenched to produce a pure glass (zero crystal) sample for test. The quenched glass was then ground and sieved to remove particles greater than 125 μm.

The mean deposition rate of the 5am (25% crystal) ash sample on coated targets is 57% compared with 43% for the 6am (40% crystal) ash. The re-melted 6am (zero crystal) ash sample gave a higher deposition rate of 62%. The adhesion rate of the 5am and 6am ash was in the 4 to 6% range with little discernable difference between the two samples. However, the re-melted 6am ash produced a much higher adhesion rate of 55% with a large amount of the 62% deposited material remaining firmly attached to the target after cool-down.

4.1.6 Eyjafjallojökull ash (58% SiO_2)

Figure 5.e shows the deposition and adhesion results for the Eyjafjallojökull trachy-andesitic ash. This sample is obtained from tephra fall from the phreatomagmatic eruption of 15 April 2010 (Gislason et. al., 2011). The ash has not been sieved, as the D_{90} value of 110 μm (Table1) suggest it is all below this size as collected.

Interestingly, at low levels of total ash delivered to the target the deposit grows at a rate of only 35 to 40% but at higher masses of delivered ash the deposition rate appears to increase significantly to around 80%. The adhesion behavior is also unusual in that an approximately constant mass of deposit remains attached to the target on cool down.

4.1.7 Mount St Helens ash (60-70% SiO_2)

Figure 5.f shows the deposition results for the Mt St Helens dacitic ash. This sample is from tephra fall deposits associated with the eruption of 18 May 1980 (Eychenne et. al., 2015). The ash was sieved to remove particles larger than 125 μm. An amount of ash was milled in a ball mill for 10 minutes at 500 rpm to create a milled ash sample. The Mt St Helens ash has a mean deposition rate of 61% with good agreement between the two experiments on coated targets. The milled ash deposition rate is 49% which is noticeably higher than the other milled ashes tested in this study, but still lower than the unmilled ash. The adhesion rate is in the range 10 to 15% while that of the milled ash is 2 to 5%.

Two experiments were carried out to evaluate the effect of maintaining the flame on the deposit for an additional 60 minutes. In both cases this resulted in a deposit mass of 52% of the calculated mass of ash captured by the flame as opposed to the 61% expected.

4.1.8 Mazama ash (70-75% SiO_2)

Figure 5.g shows the deposition results for the Mazama dacitic-rhyolite ash. This sample is obtained from re-mobilized ash from the caldera forming eruption over 7700 years ago (Bacon et. al., 2006). The sample did not require sieving as shown by the low D_{90} value in Table 1. Ash from this eruption was also used in the recent VIPR tests using a full scale, ex-service jet engine (Lekki and Woike, 2017). It should be noted that the age of this ash means it may have become hydrated which could influence its melt viscosity and sticking characteristics.

The mean deposition rate measured in the two experiments with coated targets is 54%. This compares with 57% for the uncoated target. The single test on a coated target with a reduced surface

temperature of 1050°C gave a deposition rate of 51%. The mean adhesion rate for the Mazama ash is low at 3%.

4.1.9 Summary of deposition and adhesion experiments

Table 2 presents a summary of the deposition and adhesion rates observed in the experiments by ash sample. The mean deposition rates and, where applicable, the range of results obtained for different ash types is listed. In general, this range lies within 2% of the measured deposition rate for low silica ashes (basalts and basaltic andesites) and increases to 9% for the higher silica (dacite and rhyolite) ashes. The clear exception is the Eyjafjallojökull ash which shows a very high range in the measured deposition rate which, as discussed earlier, increases significantly for high levels of ash captured in the flame.

Table 2. Summary of deposition and adhesion rates.

Ash type	Deposition; %Mean rate	Adhesion; %Mean rate
Grímsvötn	75 (1)	10 (3)
Grímsvötn - milled	*29 (1)*	*9 (3)*
Hverfjall	82 (0)	9 (7)
Hverfjall - milled	*37*	*14*
Fuego	70 (0)	4 (2)
Fuego - milled	*32*	*10*
Eyjafjallojökull	47 (34)	15 (23)
Momotombo 6am	43	6
Momotombo 5am	57 (2)	6 (1)
Momotombo 6am remelt	*62*	*55*
Mt St Helens	61 (5)	12 (2)
Mt St Helens - milled	*49 (4)*	*3 (2)*
Mazama	54 (5)	3 (2)

These results are only for the experiments with a 1250°C target and a rapid cool down. Numbers in brackets show the range for multiple tests. Bulk SiO_2 content generally increases from top to bottom.

4.2 Deposit structure, shape and density

Photographs of the deposits are shown in Figure 6. Images such as these have been used to estimate the volume and density of the deposits in Table 3, using methods described in the supplementary material C. The uncertainty of the calculated volume and density values is estimated at 10% primarily due to the potential error in determining the thickness of the lower deposit layer and the inhomogeneous nature of the deposit structure (see section 4.3). The calculated deposit densities have been compared with appropriate dense-rock-equivalent (DRE) densities (Vogel et.al., 2016)

representing a pure, structure-free glass, allowing an estimate of the porosity for the deposit. It was not possible to obtain accurate estimates of the deposit densities for the milled Hverfjall and Fuego samples due to the small mass of deposit in those experiments.

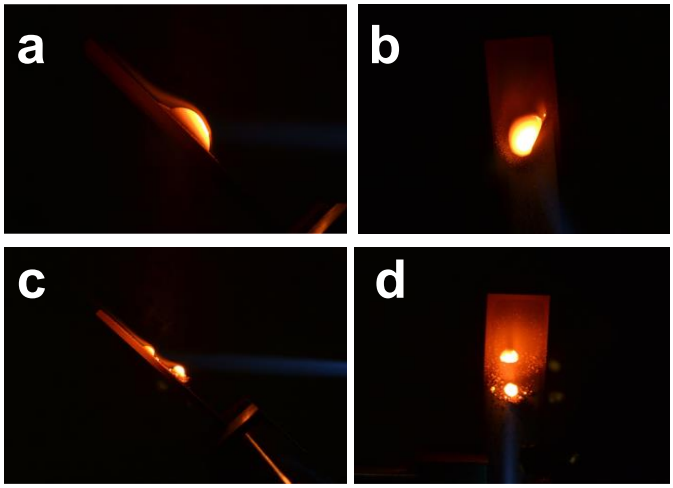

***Figure 6 a&b**; Side view and plan view of Grímsvötn ash deposit. **c&d**; Side view and plan view of Grímsvötn milled ash deposit.*

Table 3. Ash deposit volumes, density and porosity

Ash	Deposit mass (g)	Volume (mm^3)	Density (g/cm^3)		Porosity
			Deposited sample	DRE	
Hve	0.199	102	1.94	2.95	0.34
Gri	0.298	144	2.07	2.95	0.3
Gri-milled	0.064	42	1.52	2.95	0.48
Fue	0.349	216	1.62	2.9	0.44
Mom 5am	0.175	97	1.81	2.8	0.35
Mom 6am	0.131	91	1.43	2.8	0.49
Eyj	0.291	189	1.54	2.8	0.45
Msh	0.268	148	1.81	2.8	0.35
Msh-milled	0.138	83	1.66	2.8	0.41
Maz	0.171	126	1.36	2.5	0.46

4.3 Features within the deposits and targets

4.3.1 Deposits at the target interface

Figure 7 shows typical SEM images through sections of coated targets and attached deposits. As noted by Giehl et al., (2017), the deposits at the target interface is often less 'glassy' than the upper part, sometimes with a 'cindery' appearance. In most cases, a significant part of the upper glassy part

detaches from the lower (adhered) deposit along the transition zone between the cindery and glassy parts. The lower deposit layer generally varies in thickness between 10 to 20 μm and for the coated targets in this study there is clearly progressive infiltration of melt that picks out the thermal barrier columnar grain structure (Figures 7.b and 7.c). This adhered lower layer displays a number of common features; i) vesicles are usually present in the lower layer and these are particularly prevalent in the milled samples (compare Grímsvötn ash Figure 7.c with the milled sample in Figure 7.d); ii) there is generally more evidence of crystal growth within the deposit at the interface with the thermal barrier coating than elsewhere in the deposit (Figure 7.c). Energy dispersive X-ray (EDX) analysis indicates that these are usually oxide or pyroxenes; iii) Crystals are particularly large (up to 50 μm) towards the bottom of the Fuego and Mt St Helens deposits where the EDX analysis indicates these include plagioclase as well as magnetite and pyroxenes (Figure 7.e).

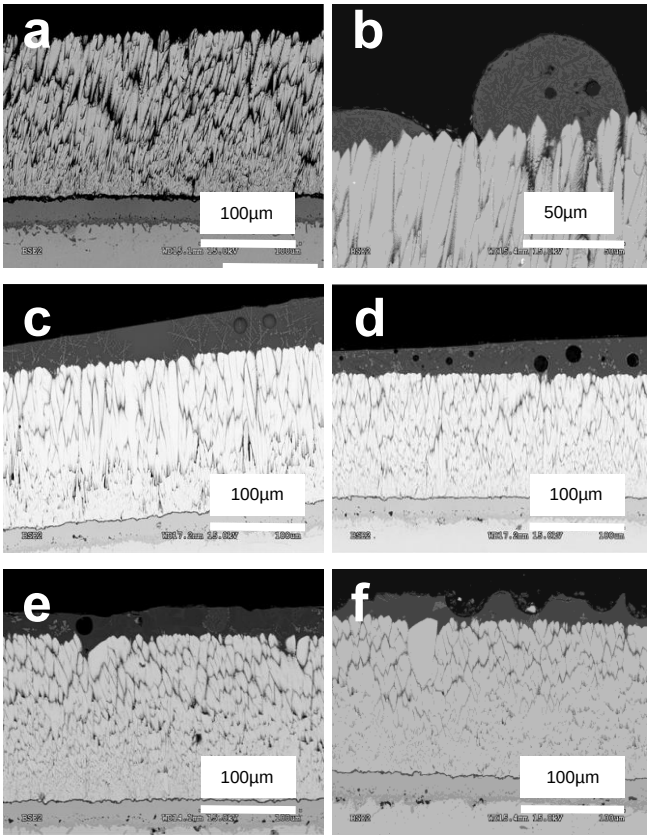

Figure 7. a; *SEM image through a section of a coated target which has not been exposed to ash. The expected columnar structure is present in the thermal barrier coating on top of an aluminium base layer (darker grey) with the Nimonic 75 substrate beneath.* ***b;*** *Isolated melt globule of Grímsvötn ash (approx. diameter 50 μm) on the periphery of the main deposit, highlighting how the molten ash has bonded to the coating and is starting to penetrate the structure and react with the TBC, similar to Mechnich et al. 2011 (see their Figure 9).* ***c;*** *Central section of Grímsvötn ash deposit with a few vesicles. Note the needle-like nature of the crystals which have clearly grown 'in situ' either during the experiment or upon cooling.* ***d;*** *Milled Grímsvötn ash deposit on top of the coating. Note there are significantly more vesicles than 7.c.* ***e;*** *Fuego ash deposit showing embedded crystals of magnetite (light crystals) and pyroxenes (darker crystals).* ***f;*** *Eyjafjallojökull ash deposit. Note the large vesicles (through which detachment of the upper deposit has taken place as the deposit cooled) and penetration of the molten ash in to the TBC structure.*

4.3.2 Detached upper deposits

Images for sections through a number of the detached deposits are shown in Figure 8. Generally, these show an inhomogeneous structure with an intermediate layer at the detachment which shows some similarity to the ash layer remaining on the target, and above this a more glassy upper layer. Features evident in these images include; i) Vesicularity, often more concentrated in the lower intermediate level (Figure 8.a), but sometimes larger, up to 0.5 mm in diameter, coalescing and moving to the upper part (Figure 8.a, 8.c & 8.f); ii) The presence of larger crystals of up to 100 μm in the Fuego (Figure 8.c) and Momotombo 6am (Figure 8.e) deposits; iii) The more silicic Mazama deposit has a high level of vesicularity but absence of crystals (Figure 8.f).

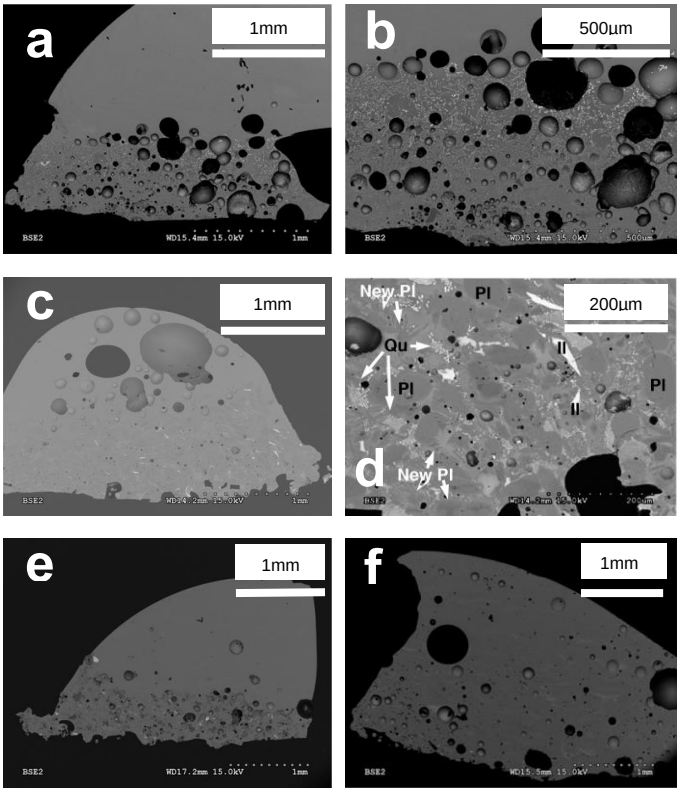

Figure 8. a; *Hverfjall ash deposit showing homogeneous upper layer and vesicular intermediate layer* ***b;*** *Close-up of the Hverfjall ash intermediate layer showing a high level of vesicularity and quench crystals. Note the larger vesicle towards the top of the intermediate layer along with a differing distribution of crystals.* ***c;*** *Fuego ash deposit showing vesicular upper layer and thick intermediate layer. Note the detachment line is through numerous vesicles.* ***d;*** *Close-up of the Fuego ash intermediate layer showing crystals of ilmenite and pyroxene.* ***e;*** *Momotombo 6am ash deposit showing a thick intermediate layer containing vesicles and crystals.* ***f;*** *Mazama ash deposit showing vesicularity spread throughout the upper layer.*

4.4 Deposit compositions

Table 4 shows the results of EDX analysis of the glass in the upper sections of the detached deposits. Also shown are the results for the re-melted Momotombo 6am ash which was checked to confirm that this sample composition is probably just in the andesitic region in Figure 2.b and that the analysis of the upper layer deposit is in reasonable agreement with this more accurately determined bulk composition. The measured composition for the upper part of the deposits, which are generally close

to 100% glass, are in approximate agreement with the 'nominal bulk compositions' given in Table 1 and Figure 2.b. The similarity between the Momotombo 6am compositions whether remelted carefully in a furnace or melted in the acetylene flame, suggests there is little to no change in composition associated with time spent in the flame. However, the more vivid yellow flame colour associated with finer milled particles could suggest metals are being lost (e.g., Na).

Table 4. EDX analysis results for the glass contained within the upper sections of detached deposits

Wt % oxide	Hve	Gri	Fue	Eyja	Mom 5am	Mom 6am	Mom 6am re-melt*	Msh	Maz
SiO_2	50.7	51.4	54.9	62.0	57.7	59.3	58.5	61.0	74.0
TiO_2	2.0	3.2	1.1	1.5	1.1	1.1	1.1	1.7	0.7
Al_2O_3	12.3	11.9	18.7	14.8	14.8	14.7	14.6	13.5	13.8
FeO	15.8	14.1	8.1	7.3	9.7	9.0	8.8	7.5	2.0
MgO	4.8	4.4	2.6	1.4	2.1	1.5	1.5	2.4	0.3
CaO	11.7	11.0	9.6	6.2	9.3	10.1	10.9	5.9	2.1
Na_2O	2.4	3.6	4.2	4.6	4.1	3.2	3.4	5.4	4.6
K_2O	0.2	0.4	0.8	1.9	1.2	1.1	1.1	1.9	2.5
Total	99.9	100.0	100.0	99.7	100.0	100.0	99.9	99.3	100.0

The values quoted are either single measurements or the mean of two measurements taken at different points in the upper section of the deposit. Where two measurements were taken the data agreed to within +/- 0.6 wt%. * This analysis is for the Mom 6am ash remelted in a furnace, not from the deposit on the target.

5. Discussion

5.1 Experimental Deposit Characteristics

5.1.1 Structure of the deposits

Based on the observations, a general mechanism for deposition formation is proposed building upon the model of Giehl et al., (2017). A schematic summary of the stages of deposit growth are shown in Figure 9.

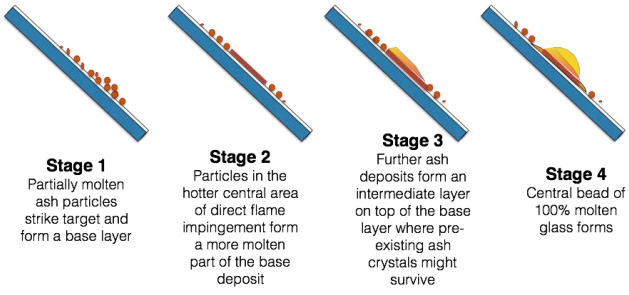

Figure 9. *Schematic illustration of the growth of the deposit on a coated target.*

The deposit begins as a base layer of molten or partially molten particles. This is surrounded by a peripheral layer of more cindery deposits that solidify on the target. Later particles impacting the central area, stick readily to the hotter molten ash surface and grow towards the flame creating an

intermediate layer of largely molten particles and vesicles. Vesicles could form from the space between individual partially molten particles (see Fig. 6.b of Giehl et al., 2017) and/or from volatiles being released from the ash. Any existing large crystals present in the ash which might have passed through the flame without melting may remain in the base and intermediate layers. Although the thermal barrier layer is designed to have insulating properties, heat is still conducted away from the flame impact area, so this base layer is maintained at a lower temperature than the 1250 °C of the impacting flame and incoming particles. This may allow new crystals to nucleate and grow (see Figures 7 and 8).

As the deposit grows the upper layer becomes thermally insulated from the target surface by the base and intermediate layers which allows a temperature close to the torch flame temperature to be maintained. This sustained high temperature is sufficient to completely melt the ash in this region including any crystals that survive the transit in the flame. The variable viscosity of this molten section of deposit will control its vesicularity at this stage. The higher viscosity of lower temperature melts (plus the interaction of any crystals) will trap vesicles inside the deposit close to the target, while the low viscosity, higher temperature melt will allow vesicles to rise, possibly coalescing on their way up (see Figure 8).

On cooling, the target and deposit contract at different rates causing thermal stresses to be created. These stresses are sufficient to fracture the deposit usually picking out the relatively inhomogeneous intermediate layer or through planes of adjacent vesicles in the base layer (see Figures 7.f and 8.c).

The deposition process described above was observed to be markedly different for some of the ashes, most notably the milled ashes from Grímsvötn, Hverfjall and Fuego and the early phases of Eyjafjallojökull deposit formation. In these cases, the initial formation of a more glassy base layer was followed by only a very gradual growth of a molten upper layer. A molten section did begin to form but then separated into smaller spheres some of which migrated away from the central impingement area, possibly due to gravity (see Figures 6.c and 6.d). It is notable that all the deposits that behaved in this way were from ash contained relatively large proportions of very fine particles (less than 3 μm). It is possible that such small particles become rapidly super-heated in the flame to much high temperatures and have very low viscosity upon reaching the target (they also exhibit a more intense yellow colour).

The observation that the milled Grímsvötn ash and the Eyjafjallojökull base layers exhibit high levels of vesicularity (Figures 7.d and 7.f) may be the result of volatiles liberated in the super-heated ash deposit. This thicker, vesicular base layer appears to then inhibit the growth of the upper layer perhaps by modifying the wetting behaviour of the intermediate section as it forms. As the Eyjafjallojökull deposit grew this effect diminished resulting in the observed increase in the deposition rate as seen in Figure 5.e.

5.1.2 Particle size and deposition rate

The size of an ash particle has a significant effect on its likelihood of deposition (Giehl et al., 2017). More efficient heat transfer should give smaller particles a higher probability of becoming molten and sticking to the target for the transit timescales of our experiments which are similar to a real jet engine (see Table 5). However, very small particles (< 6 μm; Wylie at al., 2011) can avoid impact if they are deflected and carried by the gas stream flow around our target or turn to pass through the HPNGV passage in a jet turbine. Larger particles will generally be more likely to continue towards the target due to their inertia and are not deflected sufficiently to avoid impacting the surface of the HPNGV (Bonilla et. al., 2012, Taltavull et.al, 2016). In contrast, particles that are too large to melt during their time in the flame either 'bounce off' the target (Giehl et al., 2017) or impact and become

retained in the previously molten deposit where they can experience further heat transfer in the flame. This effect will also be influenced by the ability of the molten ash to absorb the kinetic energy of the different sizes of particles. Crystals may also be kinetically more difficult to melt compared to glass, for a given particle size.

Figure 10.a shows the deposition rate (Table 2) plotted against the median diameter of the ash samples (Table 1). This plot confirms that there is a significant effect of particle size. The line shown on the chart is a least squares linear fit to the low crystal data. It should be noted that the ash samples used have no particles greater than 125 μm.

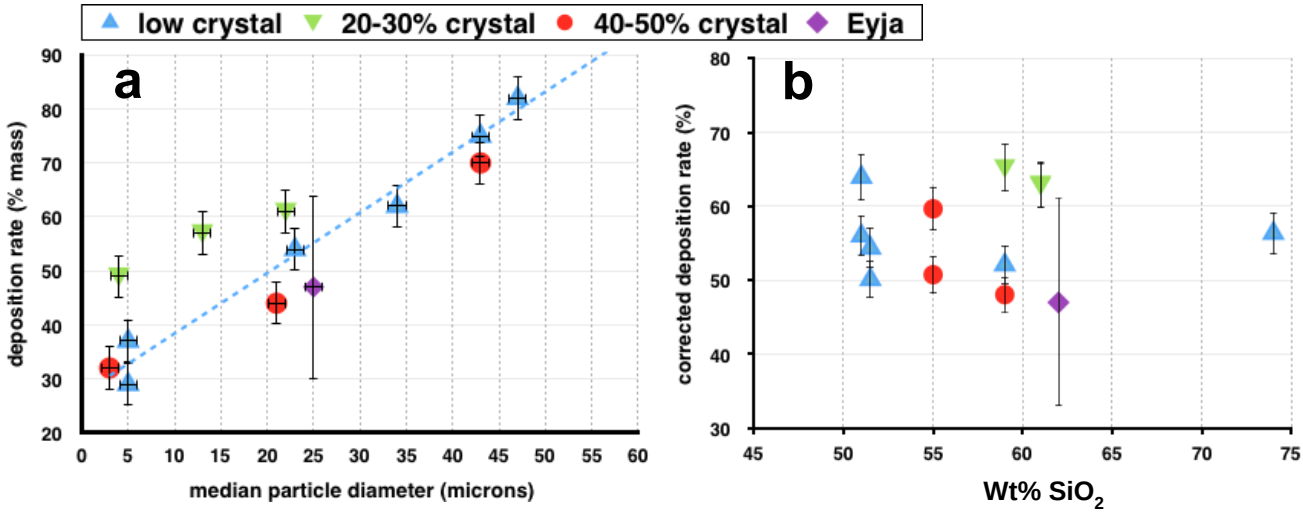

Figure 10. a; *Measured deposition rate (on coated targets) vs median particle diameter for the different types of ash tested. The blue dashed line is the least-squares linear fit to the low crystal data.* ***b;*** *Deposition rate (on coated targets) corrected to a median particle diameter of 30 μm plotted against the measured silica content of the ash deposits. The particle size correction uses the linear relationship shown in figure 10.a as described in the supplementary material E. Note: the data for Eyja ash is highlighted separately due to the much larger range of deposition rates measured as denoted by error bars.*

5.1.3 Silica and crystal content effects on deposition rate

In the light of the finding that particle size has a very significant impact upon the deposition rate, it is necessary to correct for this effect before drawing conclusions regarding silica and crystal content. To address this issue, the least-squares linear fit shown in Figure 10.a has been used to correct the measured deposition rates to a common value of median particle diameter of 30 μm as described in the supplementary material E. Figure 10.b shows the deposition rate parameter calculated in this way. All corrected deposition rates fall within the range 45% to 65% with no clear influence of silica content or crystal content.

5.1.4 Adhesion rate

Figure 11.a shows the measured coated target adhesion rate data plotted against silica content. There is considerable scatter in this data but in general the results suggest low silica basalt ashes retaining a higher level of the deposit on the targets after cool-down, although the crystal content has some effect. Supplementary material A shows a comparison of published melting temperatures for different ash samples which show a general trend of increasing melting temperature with silica content. It is likely that the increased adhesion rate of the low silica ashes is the result of either a

lower viscosity or the lower solidification temperature of these melts allowing a deeper penetration in to the coating.

The adhesion rate data could aid in understanding the likelihood of re-starting an engine after a surge has caused a flame-out situation. If ash deposits are fractured by the thermal stresses on cooling to the same extent as seen in these experiments, then the majority of a layer blocking the HPNGV could be removed, although much larger deposits may be more influenced by their internal properties and any moulding to the mechanical shapes rather than this interface effect. More realistic, scaled testing is required to draw firm conclusions including assessment of typical engine cool-down rates both after surge and after normal shut-down.

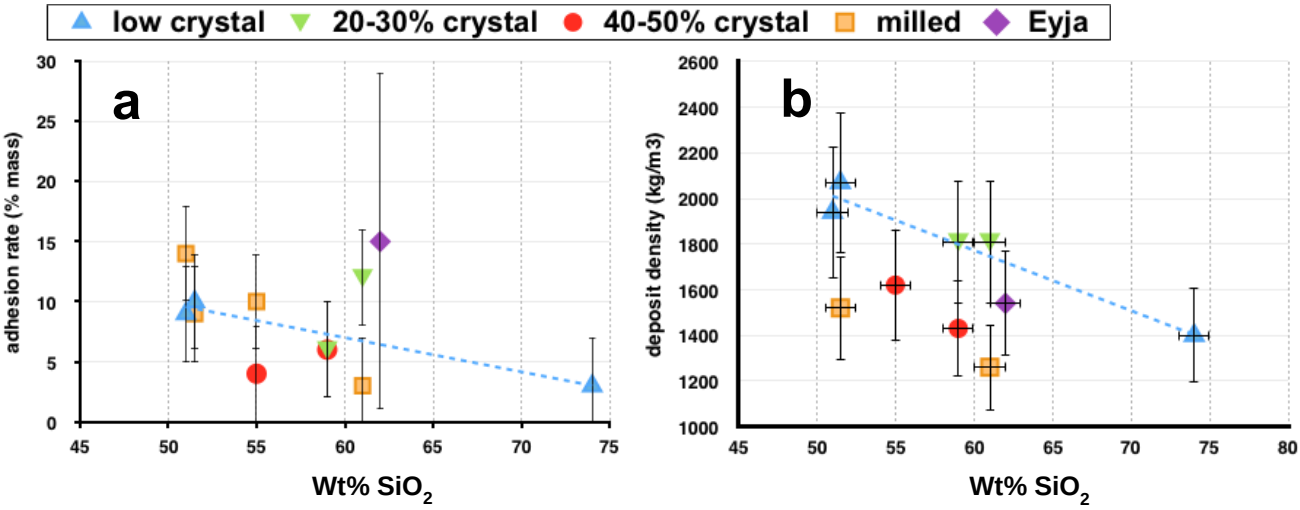

Figure 11. a; *Mean adhesion rate on coated targets vs the measured silica content of the deposits.* ***b;*** *Measured deposit density vs the measured silica content of the deposits The blue dashed lines are least-squares linear fits to the low crystal data. Error bars are shown reflecting the uncertainty in the experiments and subsequent calculations.*

5.1.5 Deposit density

Figure 11.b shows the deposit density results of Table 3 plotted against the measured silica content of the different ashes. There are large error bars associated with this data due to the level of uncertainty in the deposit volume calculations. Nevertheless, the following observations can be made with some support from the SEM images; i) there is a trend of reducing deposit density with silica content with very similar results for the low crystal and 20-30% crystal ashes; ii) the deposit densities of the 40-50% crystal ashes are 15 to 25% lower than low crystal ashes of the same silica content; ii) the deposit densities of the milled ashes are 25 to 35% lower than the unmilled ash

The deposits from high crystal content ash appear from the SEM images to exhibit a high level of porosity in either the lower layer of the detached deposit (Momotombo, Figure 8.e) or in the upper part of the deposit (Fuego, Figure 8.d). It is possible that the crystals in the molten deposit act to trap vesicles from rising to the surface due to buoyancy. It remains unclear whether the vesicles emanate from the trapped space between coalescing molten globules (see the 'porous melt' of Giehl et al., 2017) or there is some component of volatile exsolution from the ash (absorbed water or CO_2). Although the latter is more likely to be evaporated in the flame, the increase in the vesicles associated

with the finer milled ash might be related to a larger surface area (more water absorption) as 'packing' of these particles would be expected to produce less trapping of free space.

5.1.6 The influence of thermal barrier coating

Figure 5.a suggests that the deposition rates obtained with uncoated targets are generally similar to those obtained with coated targets (+/- 10%) with the exception of Grímsvötn which shows a 25% increase in the rate of deposition. However, Figure 5.b highlights a significant increase in the mass of deposit adhering to the coated targets after cool down compared with the uncoated targets. For all types of ash, the mass of deposit adhering to the uncoated targets in this study is extremely low (less than 4%). The explanation possibly involves both microstructural and thermal insulation effects.

Thermal barrier coatings made of highly refractory ceramic materials such as Zirconia (ZrO_2 often with added Y_2O_3 as in this study) are applied to turbine components using the physical vapour deposition process (PVD) which creates a columnar structure within the coating (Clarke et. al., 2012) as illustrated in Figure 7.a. This structure allows differential thermal expansion between the coating and the metal component without cracking.

The thermal insulation property of the coating impedes the flow of heat in to the metal part of the turbine which would otherwise melt at the temperatures reached during high thrust. In a real jet engine, the surface is also cooled by an internal air flow delivering cool air from the compressor which also bleeds out to form an air film on the surface via a system of mm-sized holes in the vanes and turbine blades.

In our experiments, there is a similar thermal gradient between the front of the target (1250 °C) and the back (~1000 °C), but the profile of this gradient will differ between coated and uncoated targets with more heat retained near the surface of the coated samples. These higher temperatures enhance the likelihood of a molten glass layer being maintained in contact with the target. In addition, a strong bond is formed between the deposit and the coating as a result of molten deposit entering the columnar structure of the coating (Fig 7.b).

When the silicate deposit cools, the bond between the coating and the base of the deposit allows it to withstand a higher level of thermal stress than can be tolerated by the poorly consolidated intermediate layer or the vesicular base layer (if present). The deposit therefore fractures along these features leaving a significant portion of the base layer adhering to the coated target. It should be noted that the presence of air-film holes on the surface of actual engine could act as a key which may hold more of a deposit onto the surface. Any air-film cooling hole blockage will undoubtedly lead to higher temperatures as the cooling is impeded (See Fig 8.b of Giehl et al., 2017, also Wylie et al., 2016).

Whilst the ZrO_2 has some resistance to dissolving in the silicate melt (Krämer et al., 2006), the Y_2O_3 can be drawn out and $ZrSiO_3$ crystals can form as a reaction product, weakening the TBC (Mechnich et al., 2011). Continued penetration of the molten silicate melt into the coating structure can lead to premature degradation (Levi et al., 2012). Such effects have been noted in tests of volcanic ash and other silicate materials placed on coated samples (Mechnich et al., 2011, Zhang et.al., 2018). Overall, it is clear that the presence of the coating has a significant effect on the deposit formation and retention characteristics.

5.2 Application to Jet Engine Safety

5.2.1 Experiments vs real engine conditions

Table 5 shows a comparison of key parameters for the experiments compared with the conditions in a typical gas turbine engine at cruise conditions. There is a good match between the experiment and engine parameters in terms of the temperature of the deposition surface, the residence time of the ash particles in the flame and the heating rate. One key area of divergence that needs to be considered when applying the results of these experiments to engine conditions is the velocity of the gas flow at the target.

Table 5. Comparison of experimental test parameters with typical aircraft engine conditions

Parameter	Experiment	Engine	Comments
Temperature of deposition surface (°C)	1250	1250	Matched parameter
Angle of incidence of target (HPNGV) surface	45°	10° to 80°	Angle of target chosen as mid-point in possible range
Temperature of ash at entry to flame (°C)	20	500	Ash in the engine is heated in the compression system
Mean velocity of ash particle (m/s)	15	100	Value quoted assumes gas flow accelerates from M0.1 to M0.5 in the combustor
Residence time in flame (s)	0.004	0.003	Similar order of magnitude
Gas stream temperature (°C)	1250	1400	Engine value is typical for cruise condition (Clarkson & Simpson, 2016)
Heating rate (°C/s)	3.1×10^5	3.7×10^5	Similar order of magnitude
Ambient pressure (N/m^2)	1.0×10^5	1.0×10^6	No impact on ash melting properties over this pressure range (Fagents et. al., 2013) but may influence de-gassing in molten ash

The particle temperature is not measured directly. However, the temperature within the flame significantly exceeds the melting temperature of the ash as it travels to the target (Figure 2.c). As discussed by Giehl et al. (2017), heat transfer calculations (Fedosov, 1976) suggest that particles larger than 125 μm will reach around 750 °C, particles < 80 μm will reach the 1250 °C temperature of the target and any smaller particles will get even closer to the higher flame temperature. Our measured velocities of the ash particles in the acetylene flame are in agreement with published observations and models (Giel et. al.,2017, Fedosov,1976). The velocity obtained in the experiments is significantly lower than in a gas turbine HPNGV where the flow accelerates to the speed of sound (around 400 m/s) at the minimum area position.

In a real jet engine, the sub-surface is also cooled by an internal air flow (as well as insulated by the coating), so the fact the targets in the experiments are cooler at the rear is not an unrealistic comparison, although the thermal gradient may be different. This suggests the cindery base and intermediate layers formed due to this heat loss with a more molten upper part, will also be present for actual turbine conditions.

5.2.3 Calculating deposit thickness

The key parameter of interest in determining the blockage caused within the HPNGV passages is the thickness of the deposit at the throat area location (see Figure 1.b). The results of these experiments can be used to help predict the likely deposit thickness for a given ash exposure scenario. Two key areas that need to be accounted for are the influence of particle size reduction within the engine and the time over which the ash exposure takes place.

The mass of the ash deposit can be expressed as,

$$m_{dep} = \zeta . m_{ash} . K_{size} . K_{time} \qquad \textit{\_equation (1)}$$

where; m_{dep} is the mass of the deposit, ζ is the deposition rate for the particle size distribution entering the engine, m_{ash} is the mass of ash captured by the flame (or combustor), K_{size} represents a factor applied to account for the effect of particle size reduction as the ash passes through the core of the engine, K_{time} represents a factor applied to account for the time period over which the ash exposure takes place.

By dividing by the deposit density, ρ, the volume of the deposit (V_{dep}) can be established;

$$V_{dep} = (\zeta / \rho) . m_{ash} . K_{size} . K_{time} \qquad \textit{\_equation (2)}$$

Dividing by the total HPNGV pressure surface area, $A_{NGV,}$ then gives the mean deposit thickness, h_{dep}

$$h_{dep} = (\zeta / \rho) . m_{ash} . K_{size} . K_{time} / A_{NGV} \qquad \textit{\_equation (3)}$$

The parameter A_{NGV} will be constant for a given engine type. Assuming K_{size} also remains constant then, for a given mass of ash ingested over a given length of time, the mean deposit thickness will be proportional to ζ / ρ.

5.2.4 Calculation of the size reduction factor

As ash particles pass through the engine they are subjected to repeated high-energy impacts, particularly with the compressor blades which rotate at high speeds. Engine test evidence suggests that the median particle diameters maybe as low as 5 μm by the time the ash reaches the combustor. (Dunn, 2012, Lekki and Woike, 2017). Figure 12.a shows calculated values of K_{size} assuming a five-fold reduction in ash particle size within the engine. The calculation uses the least squares fit line from Figure 10.a (See supplementary material E for more details). For example, ash with a median particle diameter of 30 μm would be expected to have a 45% lower deposition rate if it was milled to a median particle diameter of 6 μm.

5.2.5 Calculation of the exposure time factor

It is anticipated that the mass of deposited ash in an engine will be dependent upon the time it takes for the deposit to build up and the time the deposit is exposed to the high temperature and high velocity gas flow after the aircraft has passed through the ash cloud. A relationship of the following form has been proposed (Clarkson et. al., 2017),

$$dm_{dep}/dt = \zeta.dm_{ash}/dt - \lambda.m_{dep} \quad \text{\_equation (4)}$$

Where; m_{dep} is the mass of the deposit, ζ is the deposition rate, m_{ash} is the mass of ash captured by the flame (or combustor), λ (lambda) represents a constant that implies a rate of ash shedding that is proportional to the mass of the ash deposit at time, t.

Our experiments carried out with Mt St Helens ash have been used to compute a value of λ. There is a very good agreement between the two tests with a mean value of $\lambda = 2.9 \times 10^{-5}$ (1/s).

The exposure time factor, K_{time} can be calculated using this model. Equation(4) can be integrated with respect to time to give equation (5) (assuming no deposit is present at time t=0 and the rate of ash introduction to the flame, dm_{ash}/dt, is constant)

$$m_{dep}(t) = \zeta.(dm_{ash}/dt).(1-e^{-\lambda t})/\lambda \quad \text{\_equation (5)}$$

or;
$$m_{dep} = \zeta.m_{ash}.(1-e^{-\lambda T})/\lambda T \quad \text{\_equation (6)}$$

where T is the time over which the ash deposition takes place. K_{time} is therefore equal to the value, $(1-e^{-\lambda T})/\lambda T$. With the measured λ of 2.9×10^{-5} the K_{time} factor being 0.9 for a typical exposure time of 2 hours.

There are likely to be two mechanisms for deposit shedding, firstly a 'burn-off' effect which will be temperature dependent. Secondly, a 'force-off' mechanism, driven by aerodynamic effects which will be dependent upon the velocity of the gas stream over the deposit. Reference back to Table 4 shows that the gas stream temperature and particularly the gas stream velocity will be higher in an engine indicating that the value of λ could be significantly underestimated in these experiments. For example, an increase in λ by a factor of 10 would lead to a K_{time} factor of 0.45 for a 2 hour exposure.

5.2.6 Calculated deposit thickness at engine conditions

Using equation (4) together with the parameter values found in the experiments, the mean thickness of deposit for an ash dose of 2 mg/m^3 for 2 hours has been calculated and plotted in Figure 12.b. The calculated mean deposit thicknesses vary between 1.2 and 1.8 mm. Using such data, the reduction of HPNGV throat area and resultant impact on engine surge margin could be calculated by engine manufacturers (Clarkson & Simpson, 2017). Calculations suggest that the throat area reduction for a typical turbofan engine would be between 11 and 16% (see Supplementary Material F) and would roughly equate to reductions in surge margin of a similar level. While this calculation suggests that the values of thickness obtained are credible, they represent at least half of the available surge margin typically designed in to an engine (Cumpsty and Heyes, 2015). As a result they would almost certainly be considered to represent too high a safety threat.

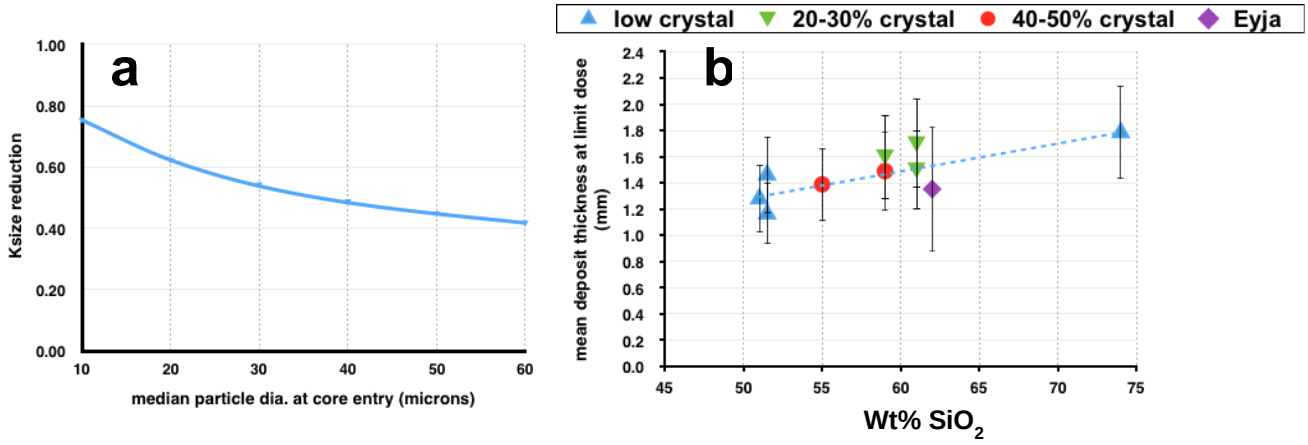

Figure 12. a; *Calculated factors to account for a 5 to 1 particle size reduction taking place as the ash passes through the engine.* ***b;*** *The calculated mean deposit thickness at the limit dose equivalent to flight for 2 hours in 2 mg/m^3 ash concentration as a function of the silica content. The blue dashed line is the least-squares linear fit to the low crystal data. Error bars are shown reflecting the uncertainty.*

As previously discussed, it is likely that the value of K_{time} used in these calculations underestimates the effect of deposit shedding from the HPNGV resulting in an overestimate of the deposit thickness in the experiments compared with the real engine scenarios. When combined with the effect of particle size reduction in a real engine, it is likely that the deposit thicknesses and consequent surge margin reduction could be reduced to around 25 to 50% of the values quoted above (i.e. 3% to 8% surge margin loss).

The calculations also assume a constant thickness of deposit build across the HPNGV surface. This assumption is also likely to result in an overestimate of the surge margin loss as experience suggests that ash deposit thickness tends to be greater towards the leading edge of the HPNGV.

6. Conclusions

The experimental set-up and methods employed in this study have provided repeatable results for each different ash sample. The measured percentage of deposited ash ranges from 29% to a maximum of 82% with Hverfjall Fires ash, a low silica basaltic ash with minimal crystal content. This is in agreement with the previous study of Giehl et al. (2017) who used a similar experimental procedure. Over the range of ash dose studied, the experiments demonstrate continuous linear accumulation in total deposit mass for each ash type, except Eyjafjallajökull which exhibits a reduced deposition rate for low levels of ash input which reaches a similar rate as the other ashes as the deposit grows.

The presence of a thermal barrier coating has been shown to increase the amount of deposit that remains on the target after it has cooled. Sections cut through the targets after deposition show ash penetration in to the coating which, at least in part, explains this observation, although the thermal insulation properties may also have an influence.

There is a clear trend of increasing deposition rate with mean particle diameter for the size range of particles tested (4 to 50 μm median diameter). These results have been used to construct a formula for predicting how the deposition rate would be affected by particle size reduction as the

ash passes through the engine. This formula has been used to correct the measured deposition rates to a common median particle diameter. After the application of this correction factor, the deposition rates fall within the range 45% to 65% and the influences of silica content or crystal content become much less significant.

A procedure has been developed for determining deposit volume from images taken during the test. Although the accuracy of this method could be improved, a trend of reducing deposit density with increasing silica content is clearly evident. The computed levels of porosity in the deposits are credible values, consistent with SEM images of sections through the deposits that reveal vesicular distributions. The SEM images of the deposits also give insight in to the deposit structure and likely build-up processes.

The measured values of deposition rate and deposit density have been used to predict the volume and mean thicknesses of deposits. This analysis suggests that variation in deposit thickness due to ash composition is of the order of +/-20% , whilst the variation due to particle size is +/- 50%. The calculated deposit thicknesses suggest that the more silicic ashes present a higher threat to engine surge margin due to the lower density caused by higher bubble concentrations producing a larger volume deposit for a given ash exposure and particle size distribution. This finding modifies the conclusions of previous studies which suggested low silica lavas (basalts and basaltic-andesites) were the most dangerous as these are more likely to adhere to the uncoated metal parts (Giehl et al. 2017). This study does confirm that low silica compositions have a higher probability of remaining adhered to TBC surfaces after engine flame-out or shutdown which is important for long term performance, degradation and servicing, particularly for coated engine parts.

A practical method has been derived to show how the results from these experiments can assist in predicting a mean thickness of ash deposit for a given ash exposure scenario. This highlights how such data could be used to more accurately underwrite an allowable ash dose. The same method could be used to help develop algorithms to detect if an engine has entered an ash cloud from engine operating data.

These experiments and analyses highlight a number of areas where further research would improve the accuracy of risk assessments for aircraft operation in volcanic ash environments and possibly leading to an increase in the safe dose limit with associated operating cost benefits,

- Experiments to quantify the value of λ and K_{time} – this would require tests at more realistic velocities and temperatures.
- A more thorough examination of the degree of size reduction that takes place as ash passes through an engine – this should cover a range of particle size and morphology.
- Further experiments to refine the deposit volume and density calculations – perhaps using more advanced instrumentation techniques to measure the profile of the hot deposit
- Improved methods of measuring or predicting the particle size distribution within the ash cloud through remote sensing and modelling.

The greater propensity for HPNGV throat area reduction by ash from more silicic volcanoes is not good news, as these are the very compositions most likely to be explosive, generating large ash clouds that can easily reach 10 km height where commercial airlines prefer to fly. Nowhere is this more important than in the ‘Pacific Ring of Fire’ where of the vast majority of damaging ash encounters have been reported (Guffanti et al., 2010). This includes South East Asia which has seen a significant growth in air traffic in recent years, in an area with a high concentration of high silica, active, explosive volcanoes.

The increased tendency for low-silica ash to infiltrate the thermal barrier coating and remain attached after engine cooling would indicate that these types of ash would be of greatest concern with respect to the ability to re-start the engine after a surge. These ashes are also likely to cause the most rapid degradation of the coatings leading to increased engine life-cycle cost.

Overall the results of our study indicate that wherever the location, it is important that the composition and nature of the ash is established soon after the eruption so that the risks represented by the ash cloud can be assessed as accurately as possible.

Acknowledgements

We thank Kathy Cashman, Hannah Buckland and Emma Liu for provided ash samples and related advice. Donovan Hawley and Charles Clapham who turned the experimental concept in to reality and Hayley Goodes, Stuart Kearns, Ben Buse and Adam Parker for their help with analytical equipment and techniques. We also thank Rory Clarkson and the Engine Environmental Impact team at Rolls-Royce plc for their guidance and for organising the manufacture of the targets at Cranfield University. We are grateful for the input from two anonymous reviewers whose comments have been incorporated in the paper. This research did not receive any specific grant from funding agencies in the public, commercial, or not-for-profit sectors.

References

Bacon, C.R. and Lanphere, M.A., 2006. Eruptive history and geochronology of Mount Mazama and the Crater Lake region, Oregon. *GSA Bulletin*, Vol.118, 1331-1359.

Bonadonna, C., Genco, R., Gouhier, M., Pistolesi, M, Cioni, R., Alfano, F., Hoskuldsson, A. and Ripepe, M., 2011. Tephra sedimentation during the 2010 Eyjafjallojökull eruption (Iceland) from deposit, radar, and satellite observations. *Journal of Geophysical Research,* Vol. 116.

Bonilla, C., Webb, J., Clum, C., Casaday, B., Brewer, E. and Bons, J.P., 2012. The Effect of Particle Size and Film Cooling on Nozzle Guide Vane Deposition. *Journal of Engineering for Gas Turbines and Power.* Vol 134.

Brown, R.J., Bonadonna, C., Durant, A.J., 2012. A review of volcanic ash aggregation. *Physics and Chemistry of the Earth Parts A/B/C.* Vol. 45&46, 65-78.

Brooker, P., 2010. Fear in a handful of dust: aviation and the Icelandic volcano. *Significance*,Vol.7, 112–115.

Buckland, H.M., Eychenne, J., Rust, A.C., Cashman, K.V., 2018. Relating the physical properties of volcanic rocks to the characteristics of ash generated by experimental abrasion. *Journal of Volcanology and Geothermal Research,* Vol. 347, 355-350.

Casadevall, T.J., 1994. The 1989-1990 Eruption of Redoubt Volcano, Alaska: impacts on aircraft operations. *Journal of Volcanology and Geothermal Research,* Vol. 62, 301-316.

Cashman, K. and Rust, A., 2017. Volcanic Ash: Generation and Spatial Variations. *Volcanic Ash,* chapter 2, DOI10.1016/B978-0-08-1000405-0.00002-1.

Clarke, D.R., Oechsner, M. and Padture, N.P., 2012. Thermal-barrier coatings for more efficient gas-turbine engines. *Materials Research Society Bulletin.* Volume 37.

Clarkson, R.J., Majewicz, E.J.E. and Mack, P., 2016. A re-evaluation of the 2010 quantitative understanding of the effects volcanic ash has on gas turbine engines. *Journal of Aerospace Engineering*, Vol. 230, 2274-2291.

Clarkson, R.J. and Simpson, H., 2017. Maximising Airspace Use During Volcanic Eruptions: Matching Engine Durability against Ash Cloud Occurrence. *NATO Public Release* STO-MP-AVT-272.

Cumpsty, N.A. and Heyes, A. L., 2015. Jet Propulsion, A simple guide to the aerodynamics and thermodynamic design and performance of jet engines. *Cambridge University Press* ISBN 978-1-107-51122-4.

Dean, J., Taltavull, C., Clyne, T.W., 2016. Influence of the composition and viscosity of volcanic ashes on their adhesion within gas turbine aeroengines, 2016. *Acta Materialia* , Vol. 109, 8-16.

Dufek, J., Huber, C. and Karlstrom, L., 2013. Magma chamber dynamics and thermodynamics. Published in *Modelling Volcanic Processes. The Physics and Mathematics of Volcanism,* edited by Fagents et.a al., Cambridge University Press, ISBN 978-0-521-89543-9.

Dunn, M.G., 2012. Operation of Gas Turbine Engines in an Environment Contaminated With Volcanic Ash. *ASME Journal of Turbomachinery*, Vol. 134 Paper 051001-1.

European Aviation Safety Agency, 2015. Certification Specifications and Acceptable Means of Compliance for Engines, CS-E amendment 4, 12 March 2015, page 1-F-2.

Eychenne, J., Cashman, K.V., Rust, A.C., Durant, A., 2015. Impact of the lateral blast on the spatial pattern and grain size characteristics of the 18 May 1980 Mount St. Helens fallout deposit. *Journal of Geophysical Research: Solid Earth*, Vol. 120, 6018-6038.

Fedosov, V.V., 1976. Particle temperature in the gas flame during powder fusion cladding. *Journal of Chemical and Petroleum Engineering*, Vol.12, 259-262.

Giehl. C., Brooker, R.A., Marxer, H. and Nowak, M., 2017. An experimental simulation of volcanic ash deposition in gas turbines and implications for jet engine safety. *Chemical Geology*, Vol.461, 160-170.

Giordano, D., Nichols, A.R.L., Dingwell, D.B., 2005. Glass transition temperatures of natural hydrous melts: a relationship with shear viscosity and implications for the welding process. *Journal of Volcanology and Geothermal Research,* Vol.142, 105-118.

Gislason, S.R., Hassenkam, T., Nedel, S., Bovet, N., 2011. Characterisation of Eyjafjallojökull volcanic ash particles and a protocol for rapid risk assessment. *Proc. Natl. Acad. Sci.* Vol.108, 7307-7312.

Gonnermann, H.M., 2015. Magma Fragmentation. *Annual Review of Earth and Planetary Sciences*. Vol.43, 431-458.

Guffanti, M, Casadevall, T, Budding, K., 2010 Encounters of aircraft with volcanic ash clouds: a compilation of known incidents, 1953–2009. *USGS* data series 545.

IATA, 2010 economic briefing, May 2010. The impact of Eyjafjallojökull's volcanic ash plume. *International Air Transport Organisation.* www. Iata.org/economics.

International Organization for Standardization, 1975. Standard Atmosphere, ISO 2533:1975.

Jiang, L-Y., Han, Y., and Patnaik, P., 2017. Characteristics of Volcanic Ash in a Gas Turbine Combustor and Nozzle Guide Vanes. *NATO Public Release*, STO-MP-AVT-272.

Kaminski, E. and Jaupart, C., 1998. The size distribution of pyroclasts and the fragmentation sequence in explosive volcanic eruptions. *Journal of Geophysical Research*, Vol.103, 29,759-29,779.

Krämer, S., Yang, J., Levi, C. G. 2006 Thermochemical Interaction of Thermal Barrier Coatings with Molten CaO–MgO–Al_2O_3–SiO_2 (CMAS) Deposits. *Journal of American Ceramic Society.,* Vol. 89, 3167–3175.

Langmann, B., Folch, A., Hensch, M., Matthias, V., 2012. Volcanic ash over Europe during the eruption of Eyjafjallojökull on Iceland, April-May 2010. *Atmospheric Environment*, Vol. 48, 1-8.

Le Bas, M. J., Le Maitre, R. W., Streckeisen, A., Zanettin, B. (1986). A chemical classification of volcanic rocks based on the total alkali-silica diagram, *Journal of Petrology*, Vol.27, 745–750.

Lee, K-I., Wu, L.T., Wu, R.T., Xiao, P., 2014. Mechanisms and mitigation of volcanic ash attack on yttria stabilized zirconia thermal barrier coatings. *Surface & Coatings Technology,* Vol.260, 68-72.

Lekki, J.D. and Woike, M.R., 2017. Vehicle Integrated Propulsion Research (VIPR) III Volcanic Ash Ingestion Testing. *NATO Public Release*, STO-MP-AVT-272.

Levi, C.G., Hutchinson, J.W., Vidal-Sétif, M-H., Johnson, C.A. 2012 Environmental degradation of thermal-barrier coatings by molten deposits. *Material Research Society Bulletin*, Vol.37, 932-941.

Liu, E.J., Cashman, K.V., Rust, A.C. and Gislason, S.R., 2015. The role of bubbles in generating fine ash during hydromagmatic eruptions. *Geology*, Vol.43, 239-242.

Liu, E.J., Cashman, K.V., Rust, A.C. and Höskuldsson, A., 2017. Contrasting mechanisms of magma fragmentation during coeval magmatic and hydromagmatic activity: the Hverfjall Fires fissure eruption, Iceland. *Bulletin of Volcanology*, Vol.79, Paper 68.

Mechnich, P., Braue, W. and Schulz, U., 2011. High-Temperature Corrosion of EB-PVD Yttria Partially Stabilized Zirconia Thermal Barrier Coatings with an Artificial Volcanic Ash Overlay. *Journal of American Ceramic Society*, Vol.94, 925-931.

Naraparaju, R., Lau, H., Lange, M., Fischer, C., Kramer, D., Schilz, U., Weber, K. 2018. Integrated testing approach using a customized micro turbine for a volcanic ash and CMAS related degradation study of thermal barrier coatings. *Surface & Coatings Technology.* Vol.337, 198-208.

Palmer, J., Ramsden, K. and Goodger, E., 1987. Compressible Flow Tables for Engineers. Macmillan Education Ltd. ISBN 0-333-44764-6.

Patnail, P.C., Chen, K. and Graham, M., 2017. Effect of Volcanic Ash on Durability and Performance of Thermal Barrier Coatings in Gas Turbine Engines. *NATO Public Release* STO-MP-AVT-272.

Prata, A.J., 2009. Satellite detection of hazardous volcanic clouds and the risk to global air traffic. *Natural Hazards*, Vol.51, 303-324.

Przedpelski, Z.J. and Casadevall, T.J., 1991. Impact of Volcanic Ash from 15 December 1989 Redoubt Volcano

Eruption on GE CF6-80C2 Turbofan Engines. *US Geological Survey Bulletin 2047* published in Proceedings of The First International Symposium on Volcanic Ash and Aviation Safety, 1991.

Rolls-Royce, 2015. The Jet Engine, 5th edition, 2015. Wiley Publishing, ISBN: 978-1-119-06599-9.

Song, W., Lavallee, Y., Hess, K-U., Kueppers, U., Cimarelli, C., Dingwell, D.B., 2016. Volcanic ash melting under conditions relevant to ash turbine interactions. *Nature Communications,* Vol.7, Paper 10795.

Song, W., Yang, S., Fukumoto, M., Lavallee, Y., Lokachari, S., Guo, H., You, Y., Dingwell, D.B., 2019. Impact interaction of in-flight high-energy molten volcanic ash droplets with jet engines. *Acta Materialia,* Vol.171, 1 June 2019, 119-131.

Sparks, R.S.J., Walker, G.P.L., 1977. The significance of vitric-enriched air-fall ashes associated with crystal-enriched ignimbrites. *Journal of Volcanology and Geothermal Research*, Vol.2, 329–341.

Swanson, S.E. and Beget, J.E., 1991. Melting Properties of Volcanic Ash. *US Geological Survey Bulletin 2047* published in Proceedings of the First International Symposium on Volcanic Ash and Aviation Safety, 1991.

Taltavull, C., Dean, J., Clyne, T.W., 2016. Adhesion of Volcanic Ash Particles under Controlled Conditions and Implications for Their Deposition in Gas Turbines. *Advanced Engineering Materials*, Vol.18, Paper 5.

Vogel, A., Diplas, S., Durant, A.J., Azar, A.S., Sunding, M.F., Rose, W.I., Sytchkova, A., Bonadonna, C., Kruger, K. and Stohl, A., 2016. Reference data set of volcanic physiochemical and optical properties. *Journal of Geophysical Research: Atmospheres*, Vol.122, 9485-9514.

Withoos, Y., 2017. The 2015-2016 Eruption of Momotombo, Nicaragua and its Wider Implications for Ash Dispersal Modelling. *University of Bristol Master of Science Thesis*, September 2017.

Wohlentz, K.H., Zimanowski, B., Büttner, R., 2013. Magma-water interactions. Published in Fagents, S.A., Gregg, T.K.P. and Lopes, R.M.C., ed., The Physics and Mathematics of Volcanism, Ch. 11, 230-249, *Cambridge University Press*, 2013.

Wylie, S., Bucknell, A., Forsyth, P., McGilvray, M., Gillespie, D.R.H., 2016. Reduction in Flow Parameter Resulting From Volcanic Ash Deposition in Engine Representative Cooling Passages. *ASME Journal of Turbomachinery,* Vol.139, Paper 3.

Zhang, B., Song, W., Guo, H., 2018. Wetting, infiltration and interaction behaviour of CMAS towards columnar YSZ coatings deposited by plasma spray physical vapour. *Journal of the European Ceramic Society,* Vol.38, 3564-3572.

Zhao, H., Yu, F., Bennett, T.D., Wadley, H.N.G., 2006. Morphology and Thermal Conductivity of Yttria Stabilised Zirconia Coatings. *Acta Materialia*, Vol.54, 5195-5207.

Supplementary Material A: Comparison of published melting temperatures of volcanic ash

Figure A1 shows data collated from three different references where measurements have been made of the melting temperatures of volcanic ash samples. The temperatures are plotted against the weight % silica content of the ashes published in the same references.

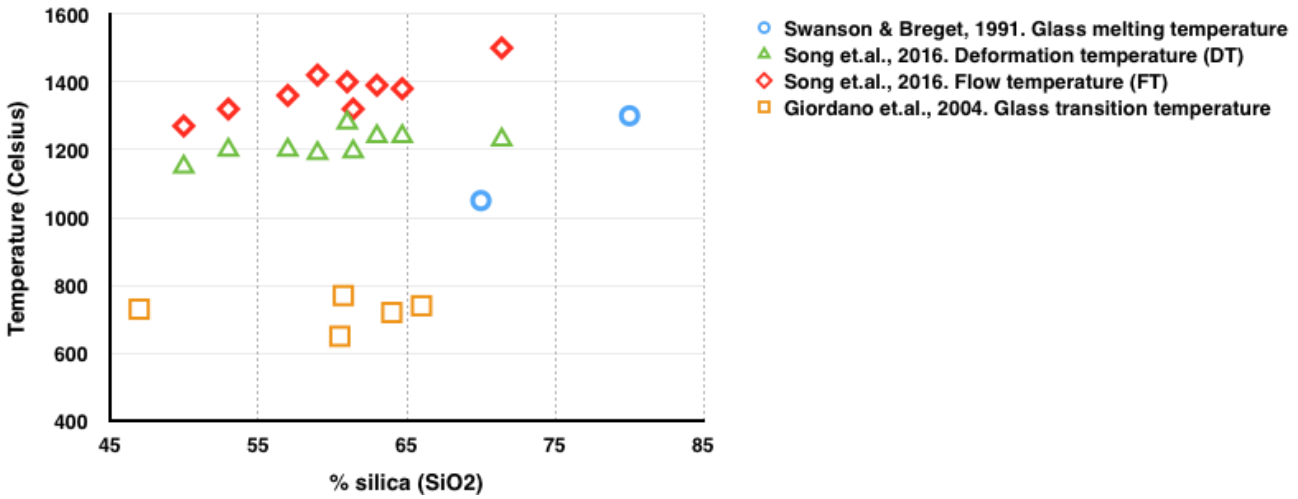

Figure A1. Collated volcanic ash melting temperatures from various references.

Using Giordano et. al., (2004) the glass transition temperature is the point at which the specific heat capacity (Cp) vs temperature curve reaches a peak denoting the relaxation of glass particles within the ash to form a liquid that will flow on a reasonable timescale (viscosity of $>10^{12}$ poise). This is the point at which 'welding' of glass particles to each other or to a hot surface can begin to take place.

In the study of Song et. al., (2016), the deformation temperature (DT) is the defined as the temperature at which a self-supported cube of compacted ash begins to physically deform. The flow temperature (FT) is the temperature at which the compacted cube of ash has become fully molten. The FT temperature will be close to the liquidus of the ash at which point all particles in the ash, including crystals, are likely to be molten. For Swanson and Breget (1991), the glass melting temperature is the liquidus of the glass particles within the ash samples tested.

This comparison highlights that there is a wide range of temperature over which the different types of particle within an ash sample begin to melt and progress to being fully molten.

There is a general trend of increasing melting temperature with increasing silica content for all the measurements shown.

Supplementary Material B: Measured ash particle size distributions

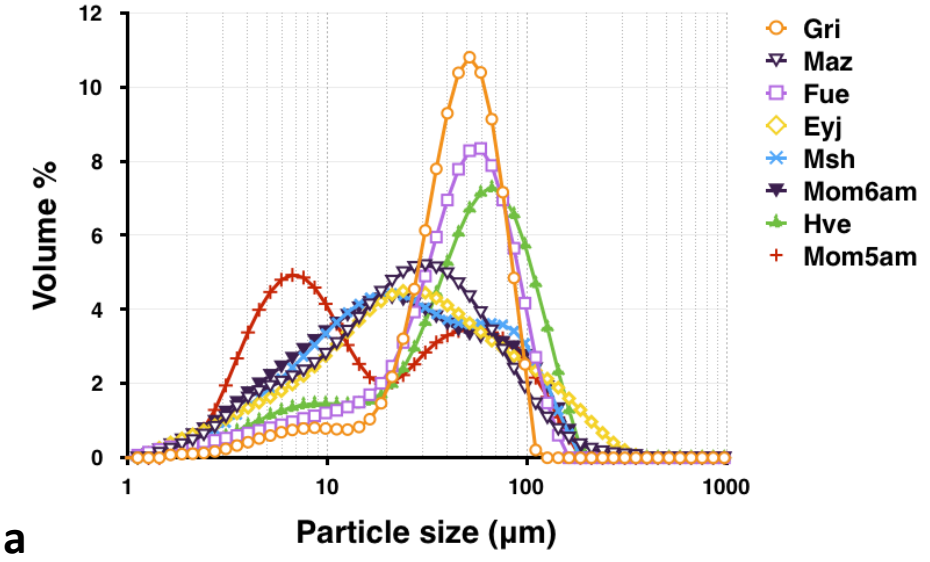

a

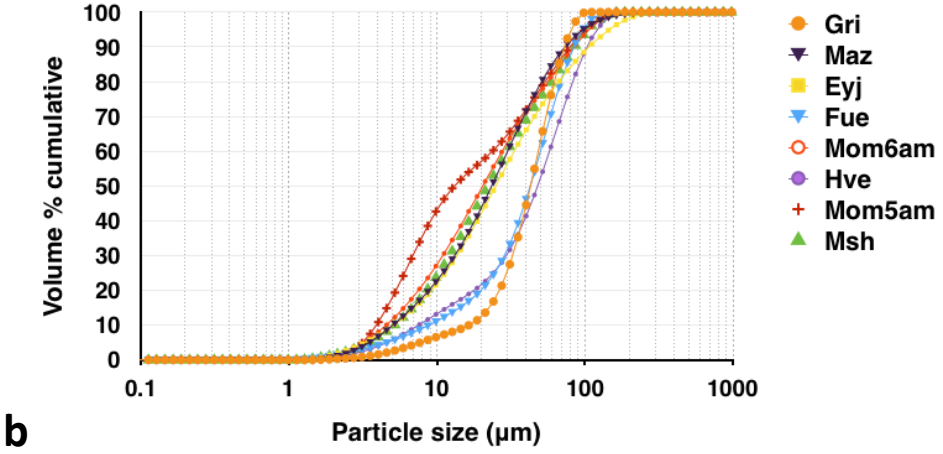

b

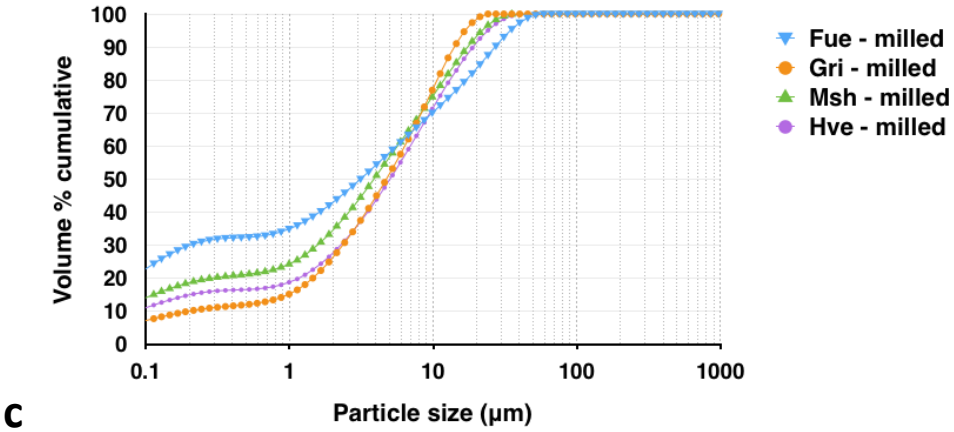

c

Figure B-1. a; *Particle size distributions of the unmilled ash samples used in the experiments (see Table 1)* ***b;*** *Cumulative particle size plots for the unmilled ash samples.* ***c;*** *Cumulative particle size plots for the milled ash samples.*

Supplementary Material C: Calculation of deposit volume

The volumes of the hot ash deposits are calculated using photographs in plan and side view as shown in Figure C-1.

Two areas are measured from the plan view by overlaying a grid which is referenced against the known dimension (width) of the target. The lower layer area (A_1) is the area within the boundary that contains the complete deposit. The upper layer area (A_2) is the area that contains the central molten upper layer of the deposit.

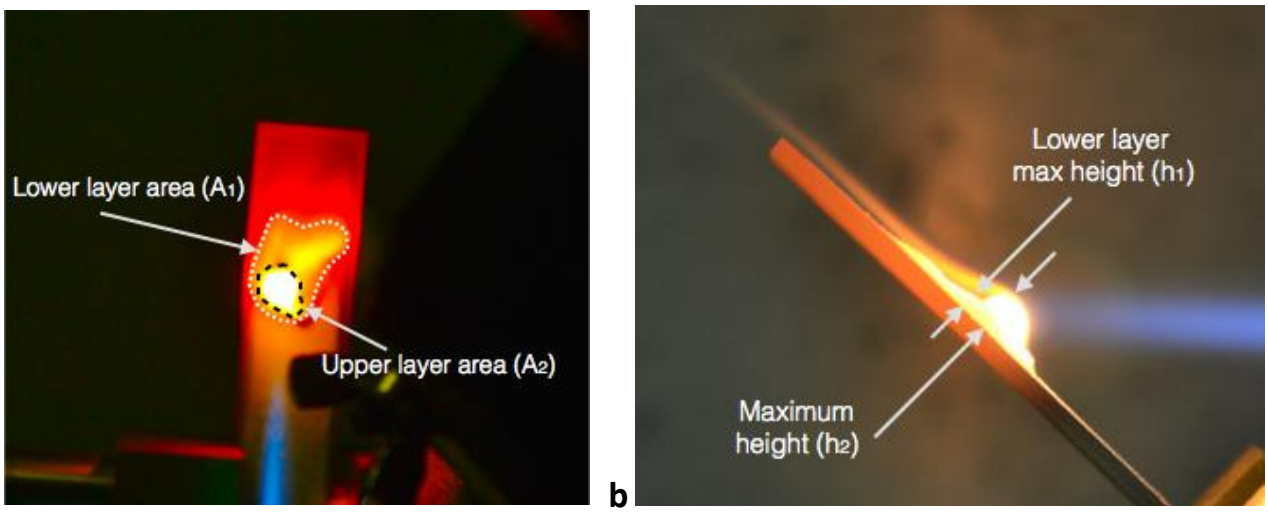

Figure C-1 a; Example plan view showing the areas of lower and upper layers of deposit (Momotombo 6am ash on coated target). **b**; Example side view showing heights of deposits used in the volume calculations.

The volume of the lower deposit (V_L) is modelled as a cylinder of deposit of base area A_2 and height h_1 plus a cone of base area ($A_1 - A_2$) and height h_1.

Therefore, $V_L = h_1 \times A_2 + (A_1 - A_2) \times h_1 / 3$

The volume of the upper layer (V_U) is modelled using the formula;

$$V_U = A_2 \times (h_2 - h_1) \times 2/3$$

For a pure hemisphere of radius, r. The above formula becomes;

$$V_U = \pi \times r^3 \times 2/3 \quad (\text{where } h_2 - h_1 = r)$$

The total deposit volume is therefore;

$$V_L + V_U = h_1 \times A_2 + (A_1 - A_2) \times h_1 / 3 + A_2 \times (h_2 - h_1) \times 2/3$$

The variation in the shape of the molten section of the deposit from almost hemispherical to a flat elliptical form is characterised by the ratio of the upper layer height ($(h_2 - h_1)$ to the square root of the upper section area (A_2).

For a pure hemisphere of radius, r; $A_2 = \pi r^2$ and $(h_2 - h_1) = r$

Therefore, $(h_2 – h_1)$ = r and the ratio $(h_2 – h_1) /\sqrt{A_2} = r/\sqrt{(\pi r^2)} = 1/\sqrt{\pi} = 0.564$

Supplementary Material D: Calculation of the equivalent limit ash dose for the experiments

Clarkson and Simpson, 2017 describes how a limiting ash dose of 15 g s/m^3 has been established for a 'notional modern turbofan engine'. This is equivalent to operating in an ash concentration of 2mg/m^3 for a period of 15/0.002 = 7500 seconds (2 hours and 5 minutes).

The Rolls-Royce Trent 900 engine is a modern turbofan engine used on the Airbus A380 aircraft. The following data is available via the Rolls-Royce.com website,

Trent 900 Take-off airflow (W_{total}) = 1200 kg/s,
Bypass ratio (BPR) = 8.4,
Overall pressure ratio (OPR) = 39

Bypass ratio is defined as the mass flow of air bypassing the core of the engine (W_f) divided by the mass flow of air entering the core engine compressors (W_c).

i.e. $BPR = W_f / W_c = (W_{total} - W_c) / W_c$

Solving for W_c gives; $W_c = W_{total} / (BPR \times (1+1/BPR) = 1200 / (8.4 \times (1+1/8.4) = 127.7$ kg/s

There is, therefore, 127.7 kg/s of air mass flow entering the core compressor section of the engine at take-off.

The operating point of the engine compression system is governed by the compressor characteristic as shown in figure 1d. This is a non-dimensional characteristic whereby the parameter ($W_c\sqrt{T}/P$) remains constant for a given throttle setting. Where T is the total temperature of the flow in to the compressor and P is the total temperature at entry to the compressor. (Cumpsty and Heyes, 2015)

The value of ($W_c\sqrt{T}/P$) at take-off can be computed as $127.7 \times \sqrt{288} / 1.013 \times 10^5$ using standard values for sea level temperature and pressure in S.I. units (International Organization for Standardization, 1975). This gives a value of $W_c\sqrt{T}/P = 0.0213$ at take-off.

At cruise conditions of 10,000m altitude, Mach 0.83, assuming the engine is throttled back to a value of $W_c\sqrt{T}/P$ 10% lower than at take off (0.0213×0.9) = 0.0191

Standard atmospheric conditions at 10,000m are, ambient (static) temperature= 223K, ambient pressure= 2.65×10^4 N/m^2 (International Organization for Standardization, 1975)

Compressible flow tables for a Mach No. of 0.83 gives a total/ static temperature ratio of 1.14 and a total/static pressure ratio of 1.57. (Palmer et.al.,1987)

Therefore T = $1.14 \times 223 = 254$K, $P = 1.57 \times 2.65 \times 10^4 = 4.16 \times 10^4$ N/m^2

$W_c\sqrt{T}/P = 0.0191 = W_c \times \sqrt{254} / 4.16 \times 10^4$

Therefore W_c = 49.8 kg/s at cruise conditions

The density of air at 10000m is 0.413 kg/m^3 (International Organization for Standardization, 1975)

Therefore the volume of air ingested in to the core compressors is 49.8 / 0.413 = 120 m^3/s

So, at the limit dose of 15 gs/m^3, the total mass of ash ingested in to the core compressors of the engine is;

15 x 120 = 1800g (1.8 kg).

Not all the air/ash mixture that passes through the compressors will enter the combustor as air is bled from the compressors for cooling the hot parts of the engine. Bleed air also supplies the aircraft pressurisation system. A typical value for the total amount of air bled from the compressor is 20% (Cumpsty and Heyes, 2015). It is reasonable to assume that a similar mass of ingested ash is taken away in the bleed air, which of course causes other problems for the engine and aircraft systems (Dunn, 2012).

This bleed effect reduces the mass of ash at the limit condition to 1.44 kg.

The mass of ash calculated in this way is scaled to the experimental size by comparing the deposition area for the hot ash/air stream. In the engine this area is taken to be the total surface area of the HPNGV pressure surface (A_{NGV}) which, by scaling publicly available images, is estimated to be;

70mm span x 70mm chord x 40 (No. of HPNGVs) this gives an area of 196000 mm^2

The appropriate area of the target used for scaling is the impingement area of the torch on to the target which is taken to be the mean of the plan areas of the central layers of the deposits. This value of 37 mm^2 equates to a flame diameter of 6mm impacting at 45^O which is consistent with the geometry of the target and torch.

The scaling ratio for the experiments is therefore, 37:196000 or 1:5300.

The mass of ash at the experiment scale equivalent to the limit dose is therefore;

1.44 kg / 5300 = 0.00027 kg = 0.27g

Supplementary Material E: Calculation of size reduction factor, K_{size}

Figure 10.a in the main text shows the least-squares linear fit for low crystal ashes (blue dashed line). The higher crystal ashes follow a similar trend albeit with higher scatter.

The equations of the line is;

$$\text{deposition rate,} \quad \zeta\,(\%) = 1.21 \times D_{50} + 27.2$$

where D_{50} is the median particle diameter in microns (μm).

To account for a reduction in particle size as the ash passes through the size reduction factor, K_{size} can be estimated by the following formulae;

$$K_{size} = (1.21 \times D_{50\,out} + 27.2) / (1.21 \times D_{50\,in} + 27.2)$$

Where; $D_{50\,in}$ = median particle diameter at entry to the engine

$D_{50\,out}$ = median particle diameter at entry to the combustor

It should be noted that the above results are only valid for ash particle size distributions with no particles greater than 125μm.

In the absence of better data, $D_{50\,out}$ can be approximated as $D_{50\,in}$ /5. This ratio has been used to establish figure 12.a.

The same formulae have been used to correct the measured deposition rate data to a common particle size of 30μm (figure 10.b). The following correction factors are applied in this case;

$$\zeta_{30} = \zeta_{meas} \times (1.21 \times 30 + 27.2) / (1.21 \times D_{50\,meas} + 27.2)$$

where, ζ_{30} is the deposition rate corrected to 30μm

ζ_{meas} is the measured deposition rate

$D_{50\,meas}$ is the median particle diameter in the ash sample tested.

Supplementary Material F: Calculation of surge margin reduction

During cruise and high power engine operation the HPNGV operates in a choked condition where sonic (Mach 1) conditions are achieved. At this point no further increase in mass flow through the HPNGV passages can be achieved and the quasi-non-dimensional flow parameter, Q reaches a maximum (Cumpsty & Heyes, 2015).

For gas turbine combustion products, where the ratio of specific heats, γ is 1.33, the value of Q at Mach 1 is 0.040 in S.I. units. (Palmer et. al., 1987)

Q is defined as $W\sqrt{T}/P.F$, where F is the cross-sectional area of the flow and the other parameters are as defined in Supplementary Material D.

The flow area of the HPNGV (F_{NGV}) can therefore be found by the formula;

$F_{NGV} = W\sqrt{T}/P.Q$

From Supplementary Material D: W_c = 49.8 kg/s at cruise conditions. As approximately 20% of the core flow is lost due to bleed, W at the HPNGV will be 0.8 x 49.8 = 40.0 kg/s.

The total pressure, P at the HPNGV will be the pressure at inlet to the compression system multiplied by the overall pressure ratio (OPR) of the engine at cruise – which will be assumed to be 80% of the peak OPR of the engine (39).

Therefore, $P = 4.16x10^4 \times 39 \times 0.8$ N/m^2 $= 1.3 \times 10^6$ N/m^2

The temperature at the HPNGV is 1400^0C = 1673K (see Table 5)

F_{NGV} is therefore, $W\sqrt{T}/P.Q = 40.0 \times \sqrt{(1673)} / 1.3 \times 10^6 \times 0.04 = 0.031$ m^2

The area reduction (F_{dep})created by a deposit of mean thickness, h will be given by;

F_{dep} = h x No. of NGVs x Span of NGVs = h x 40 x 0.07 (m^2) (see Supplementary Material D)

For a 1mm (0.001m) thick mean deposit,

F_{dep}= 0.001 x 40 x 0.07 = 0.0028 m^2

The percentage reduction in flow area for a 1mm deposit is therefore 0.0028 / 0.031 = 9%

In response to this reduction in flow area, the engine will re-match such that the value of Q will remain at the choked value of 0.04. In reality there will be changes in all parameters W, T and P to achieve this condition (as illustrated in figure F-1). However, as percentage changes in mass flow will

be small (at least for an engine controlled on compressor RPM) and temperature change will be a small effect as it is square-rooted, To a first order the percentage reduction in flow area will be balanced by an equivalent increase in pressure. This percentage increase in pressure is, by definition, the surge margin loss as a result of the deposit formation.

Therefore, for the range of deposit thicknesses predicted from these experiments (1.2 to 1.8 mm, see figure 12.b) a surge margin loss of 11 to 16% could be expected.

As discussed in the text, the application of a realistic size reduction factor, K_{size} (0.55 for ash with a median particle diameter of 30μm at compressor entry), and time exposure reduction factor, K_{time} (between 0.9 and 0.45), the expected surge margin loss would be reduced to 25 to 50% of these values – i.e. 5.5% to 8% surge margin loss at the limit dose.

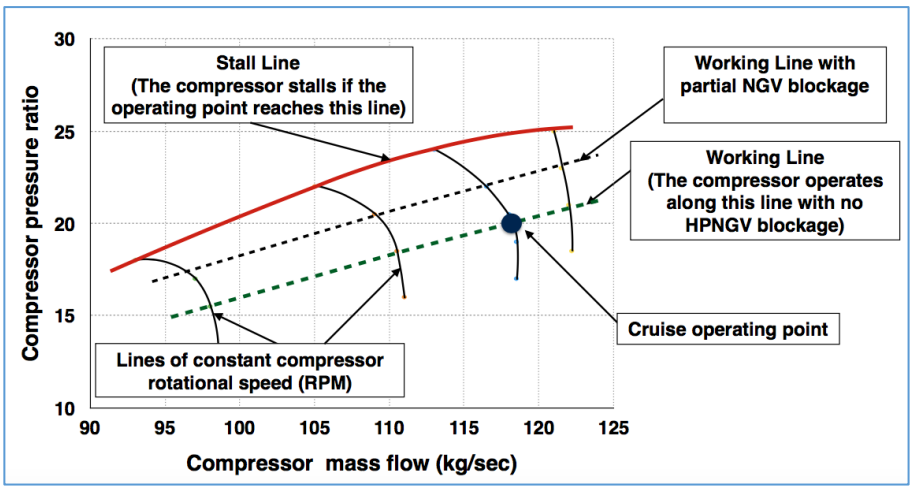

Figure F-1 *A typical compressor pressure ratio vs flow characteristic map (adapted from Cumpsty & Heyes, 2015) highlighting how the working line of the engine changes as a result of partial HPNGV blockage.*